

1 **Radiation fog properties in two consecutive events under polluted and clean**  
2 **conditions in the Yangtze River Delta, China: A simulation study**

3 Naifu Shao<sup>1</sup>, Chunsong Lu<sup>1</sup>, Xingcan Jia<sup>2</sup>, Yuan Wang<sup>3</sup>, Yubin Li<sup>1</sup>, Yan Yin<sup>1</sup>, Bin Zhu<sup>1</sup>,  
4 Tianliang Zhao<sup>1</sup>, Duanyang Liu<sup>4</sup>, Shengjie Niu<sup>1,5</sup>, Shuxian Fan<sup>1</sup>, Shuqi Yan<sup>4</sup>, Jingjing Lv<sup>1</sup>

5 <sup>1</sup>Key Laboratory for Aerosol-Cloud-Precipitation of China Meteorological Administration/Collaborative  
6 Innovation Centre on Forecast and Evaluation of Meteorological Disasters (CIC-FEMD), Nanjing University of  
7 Information Science & Technology, Nanjing 210044, China

8 <sup>2</sup>Institute of Urban Meteorology, China Meteorological Administration, Beijing 100089, China

9 <sup>3</sup>Collaborative Innovation Centre for Western Ecological Safety, Lanzhou University, Lanzhou 730000, China.

10 <sup>4</sup>Key Laboratory of Transportation Meteorology of China Meteorological Administration, Nanjing Joint Institute  
11 for Atmospheric Sciences, Nanjing, 210041, China

12 <sup>5</sup>College of Safety Science and Engineering, Nanjing Technology University, Nanjing 210009, China

13 *Correspondence to:* Chunsong Lu (luchunsong110@gmail.com)

14

15 **Abstract.** Aerosol–cloud interaction (ACI) in fog and planetary boundary layer (PBL)  
16 conditions play critical roles in the fog life cycle. However, it is not clear how ACI in the first  
17 fog (Fog1) affects the PBL, and subsequently affects ACI in the second fog (Fog2), which is  
18 important to understand the interaction between ACI and the PBL as well as their effects on fog  
19 properties. To fill this knowledge gap, we simulate two successive radiation fog events in the  
20 Yangtze River Delta, China, using the Weather Research and Forecasting model coupled with  
21 Chemistry (WRF-Chem). Our simulations indicate that the PBL conditions conducive to Fog2  
22 formation are affected by ACI with high aerosol loading in Fog1; subsequently, the PBL  
23 promotes ACI in Fog2, resulting in a higher liquid water content, higher droplet number  
24 concentration, smaller droplet size, larger fog optical depth, wider fog distribution, and longer  
25 fog lifetime in Fog2 than in Fog1. This phenomenon is related to the following physical factors.  
26 The first factor involves meteorological conditions conducive to Fog2 formation, including low  
27 temperature, high humidity, and high stability. The second factor is the feedbacks between

28 microphysics and radiative cooling. A higher fog droplet number concentration increases the  
29 liquid water path and fog optical depth, thereby enhancing long-wave radiative cooling and  
30 condensation near the fog top. The third factor is the feedbacks between macrophysics,  
31 radiation, and turbulence. A higher fog top presents stronger long-wave radiative cooling near  
32 the fog top than near the fog base, which weakens temperature inversion and strengthens  
33 turbulence, ultimately increasing the fog-top height and fog area.

34 In summary, under polluted conditions, ACI postpones the dissipation of Fog1 owing to  
35 these two feedbacks and generates PBL meteorological conditions that are more conducive to  
36 the formation of Fog2 than those prior to Fog1. These conditions promote the earlier formation  
37 of Fog2, further enhancing the two feedbacks and strengthening the ACI in Fog2. Our findings  
38 are critical for studying the interaction between aerosols, fog, and the PBL; moreover, they  
39 shed new light on ACI.

## 40 **1 Introduction**

41 Fog comprises water droplets or ice crystals suspended above the ground (WMO, 1992). This  
42 results in low visibility, which affects the human health, transportation, and power systems (Niu  
43 et al., 2010). Uncertainties exist in fog forecasting (Zhou and Du, 2010; Zhou et al., 2011). An  
44 important reason is that the physical processes of fog remain unclear because many processes  
45 (aerosol activation, condensation, radiation, and turbulence) occur simultaneously and interact  
46 with each other nonlinearly (Haefelin et al., 2010), which affects fog properties (Mazoyer et  
47 al., 2022) and impedes related parameterisation (Poku et al., 2021). To better understand the  
48 physical processes of fog, comprehensive studies based on observations and simulations have  
49 been conducted to better understand the physical processes of fog (Fernando et al., 2021;  
50 Gultepe et al., 2014; Guo et al., 2015; Hammer et al., 2014; Liu et al., 2011; Price et al., 2018;  
51 Shen et al., 2018; Wang et al., 2021). The critical roles of aerosols and planetary boundary layer

52 (PBL) in these processes have been shown (Boutle et al., 2018; Niu et al., 2011; Quan et al.,  
53 2021).

54 Since fog is a special type of cloud (Guo et al., 2021; Kim and Yum, 2010, 2013; Wang et  
55 al., 2023), aerosol–fog interaction is expected to share similarities with aerosol–cloud  
56 interaction (ACI). The ACI in fog reflects the response of fog properties to changes in aerosol  
57 loading. Studies on ACI revealed that increasing aerosol loading increased cloud droplet  
58 concentration, thereby increasing the cloud optical depth under a constant liquid water content  
59 (LWC) (Garrett and Zhao, 2006; Twomey, 1977; Wang et al., 2013; Wang et al., 2018; Zhao  
60 and Garrett, 2015). Various continental fog observation projects showed that fog microphysical  
61 properties were significantly affected by aerosol loading (Mazoyer et al., 2019; Niu et al., 2011;  
62 Quan et al., 2011; Wang et al., 2021). For instance, in polluted fog observations, Quan et al.  
63 (2011) found that the fog droplet number concentration ( $N_d$ ) was higher than  $1,000 \text{ cm}^{-3}$  and  
64 effective radius ( $R_e$ ) was approximately  $7 \text{ }\mu\text{m}$  in the North China Plain. In clean fog  
65 observations, Wang et al. (2021) showed that  $N_d$  was smaller than  $100 \text{ cm}^{-3}$  and  $R_e$  was  
66 approximately  $9 \text{ }\mu\text{m}$  in the tropical rainforest in Xishuangbanna, China. Several simulation  
67 studies reproduced these observations, and demonstrated the complex impact of ACI on fog  
68 micro- and macrophysics (Jia et al., 2019; Maalick et al., 2016; Stolaki et al., 2015; Yan et al.,  
69 2020). Regarding fog microphysics, increasing aerosol loading in the simulations increased  $N_d$   
70 and LWC due to increased activation and condensation (Jia et al., 2019; Stolaki et al., 2015;  
71 Yan et al., 2020). Regarding fog macrophysics, several modelling studies reported that  
72 increasing aerosol loading increased the fog-top height (Jia et al., 2019; Stolaki et al., 2015)  
73 and prolonged the fog lifetime by delaying its dissipation (Quan et al., 2021; Yan et al., 2021).

74 Furthermore, previous studies found that meteorological conditions played crucial roles in  
75 ACI as well as cloud macro- and microphysics (Ackerman et al., 2004; Kumar et al., 2017;  
76 Kumar et al., 2021; Liu et al., 2019; Liu et al., 2020; Toll et al., 2019). Similarly, studies on fog

77 showed that ACI was affected by meteorological conditions in the PBL (e.g., radiation,  
78 thermodynamics, and dynamics), which further affected fog micro- and macrophysics  
79 (Haeffelin et al., 2010). Previous studies showed that radiative cooling was an important factor  
80 in temperature inversion that provided stable conditions for fog formation (Fitzjarrald and Lala,  
81 1989; Holets and Swanson, 1981; Roach et al., 1976). According to Zhou and Ferrier (2008),  
82 turbulence may suppress or deepen the fog-top height, which was related to the critical  
83 turbulence coefficient. The critical turbulence coefficient was the turbulence threshold for  
84 diagnosing whether turbulence suppressed fog or not. When the turbulence intensity within the  
85 fog did not exceed the critical turbulence coefficient, the fog persisted; however, when it  
86 surpassed its threshold, the fog dissipated (Zhou and Ferrier, 2008). When temperature  
87 inversion was weak, excessive vertical turbulent mixing delayed fog formation (Maronga and  
88 Bosveld, 2017). However, when temperature inversion was sufficiently strong, vertical  
89 turbulent mixing at the middle and fog base increased the fog-top height, as suggested by  
90 observations (Ye et al., 2015) and simulations (Porson et al., 2011). Consequently, turbulence  
91 may impact fog macrophysics. Moreover, aerosols were reported to affect turbulence, thereby  
92 impacting fog macrophysics (Jia et al., 2019; Quan et al., 2021). A qualitative analysis,  
93 conducted in a previous study, revealed that aerosols promoted turbulence and horizontal  
94 distribution because of weaker temperature inversion (Jia et al., 2019).

95 Previous studies typically focused on either a single fog event or analysed multiple fog  
96 events statistically; however, several studies noted that LWC,  $N_d$ , and liquid water path (LWP)  
97 in a latter fog event exhibited larger values compared to those for the preceding fog event (Quan  
98 et al., 2011; Wærsted et al., 2017). What are the physical mechanisms behind the property  
99 changes during two successive fog events? Furthermore, which fog event has macro- and  
100 microphysical properties that are more sensitive to aerosol loading, i.e., experiencing a stronger  
101 ACI? What are the mechanisms underlying the interactions between ACI and the PBL? To

102 answer these questions, two successive radiation fog events in the Yangtze River Delta (YRD)  
103 region of China are simulated in this article using the Weather Research and Forecasting model  
104 coupled with Chemistry (WRF-Chem). The two fog events provide an excellent opportunity to  
105 investigate ACI under polluted conditions as a chain. This involves analysing how high aerosol  
106 loading affects properties in the first fog event, how the properties in the first polluted fog event  
107 affect radiation and PBL structure, and finally, how radiation and the PBL affect properties and  
108 ACI in the second fog event under polluted conditions. Additionally, since fog is a special type  
109 of cloud near the ground, studying the evolution of ACI in fog aids in examining the progression  
110 of ACI in cloud, which is critical for climate prediction (Boutle et al., 2018; Vautard et al.,  
111 2009) .

112 The rest of the article is organized as follows. Section 2 presents descriptions of the two  
113 successive fog events, experimental design, and data source. Section 3 presents simulation  
114 evaluation. Section 4 shows larger aerosol-induced changes in Fog2 than in Fog1. Section 5  
115 presents the physical mechanisms underlying the larger aerosol-induced changes in Fog2 than  
116 in Fog1. Finally, Section 6 summarises the conclusions of this study.

## 117 **2 Experimental design and data source**

118 Here, we study how radiation fog properties are affected by high aerosol loading and PBL  
119 meteorological conditions in two successive events in the YRD region. Before fog events in the  
120 YRD, the PM<sub>2.5</sub> mass concentration was over 100  $\mu\text{g m}^{-3}$  due to anthropogenic emissions (Zhu  
121 et al., 2019). On 26 and 27 November 2018, two successive radiation fog events occurred in  
122 northern YRD. The first fog event is called Fog1, and the second one is called Fog2. Ground-  
123 based observations at the Nanjing site (32.2 °N 118.7 °E) show that two fog events (visibility  
124 < 1,000 m) are accompanied by high relative humidity, low temperature, and weak wind speed  
125 (Fig. 1). As shown in Fig. S1, the surface is controlled by a high–pressure system with cold and

126 moist air in northern YRD at 20:00 local standard time (LST) (LST = Universal Time  
127 Coordinated + 8 h) on 26 and 27 November 2018. WRF-Chem (version 4.1.3) is used to  
128 simulate the two successive radiation fog events. WRF-Chem couples physical and chemical  
129 processes; therefore, it has been widely used to study ACI (Jia et al., 2019; Lee et al., 2016;  
130 Yan et al., 2020; Yan et al., 2021). The model is integrated from 14:00 LST on 24 November  
131 2018 to 14:00 LST on 27 November 2018, with the first 24 hours regarded as the spin-up time.  
132 As shown in Fig. S2, the model is configured using three nested domains, and all domain centres  
133 are located in Nanjing. The three nested domains are  $90 \times 122$ ,  $118 \times 142$ , and  $130 \times 154$  grid  
134 cells with resolutions of 27, 9, and 3 km, respectively. The simulation area covers the major  
135 weather system affecting the YRD. The model includes 36 vertical levels, of which 17 layers  
136 are located at the lowest 500 m above the ground level. Moreover, Yang et al. (2019) noted a  
137 better fog simulation performance when the bottom layer was 8 m above the ground since this  
138 layer affected the fog and surface flux interaction. Consequently, in this study, we set the bottom  
139 layer of the model to 8 m. The model is driven by the National Centre for Environmental  
140 Prediction (NCEP) Final (FNL)  $1^\circ \times 1^\circ$  reanalysis data (<https://rda.ucar.edu/datasets/ds083.2/>)  
141 (Ding et al., 2019; Jia et al., 2019). The Multiresolution Emission Inventory for China (MEIC)  
142 database (<http://meicmodel.org>) is used for anthropogenic emissions in the model (Li et al.,  
143 2017a; Zheng et al., 2018).

144 Table 1 lists the parameterisation schemes of physical processes used in this study. The  
145 microphysics scheme is Morrison (Morrison et al., 2005) coupled with the activation scheme  
146 (Abdul-Razzak, 2002). The PBL scheme is MYNN2.5 (Nakanishi and Niino, 2009).  
147 Turbulence is parameterised in the MYNN2.5 scheme and there is also a sub-grid cloud  
148 parameterisation (Chaboureau and Bechtold, 2002) in the MYNN2.5 scheme. The radiation  
149 schemes are coupled with the aerosol–cloud–radiation interactions. The long- and short-wave  
150 radiation schemes are RRTMG (Iacono et al., 2008) and Goddard (Matsui et al., 2020),

151 respectively. The cumulus scheme is Grell 3D (Grell and Dévényi, 2002). The chemistry  
152 schemes are MOSAIC-4 bins (Zaveri et al., 2008) and CBMZ (Zaveri and Peters, 1999).

153 For model evaluation, meteorological data are retrieved from the China Meteorological  
154 Administration (<http://www.nmic.cn/>). The cloud product (level 2 full-disk cloud property data)  
155 from the Himawari-8 geostationary satellite is used (Bessho et al., 2016; Iwabuchi et al., 2018)  
156 (<https://www.eorc.jaxa.jp/tree/index.html>). The quality of the Himawari cloud product is  
157 reliable because this product has been evaluated against the Moderate Resolution Imaging  
158 Spectroradiometer (MODIS) (Bessho et al., 2016; Letu et al., 2020) and cloud profiles from  
159 aircraft measurements (Zhao et al., 2020). Spatial resolution of the Himawari cloud product is  
160  $0.05^{\circ} \times 0.05^{\circ}$  (Yang et al., 2020).  $PM_{2.5}$  mass concentration data are obtained from the Ministry  
161 of Environmental Protection (<https://quotsoft.net/air/>).

162 To investigate the aerosol-induced changes in fog macro- and microphysics, one control  
163 run and two sensitivity tests are conducted: EXP1, EXP2, and EXP3, respectively. High and  
164 low emissions indicate polluted and clean conditions, respectively. The differences indicate the  
165 aerosol effect on fog properties. In EXP1, the emission intensity is obtained directly from the  
166 MEIC database to simulate fog under polluted conditions. In EXP2, the emission intensity is  
167 multiplied by 0.05 to simulate fog under clean conditions, as described by Jia et al. (2019) and  
168 Yan et al. (2021). In EXP3, Fog1 occurs under clean conditions (5% of emission from the MEIC  
169 database) and Fog2 occurs under polluted conditions (the default emission from the MEIC  
170 database). According to Fog1 dissipation time, clean conditions change to polluted conditions  
171 at 12:00 LST on 26 November 2018. Compared with the difference between EXP1 and EXP2,  
172 the difference between EXP3 and EXP2 reveals whether the fog properties and ACI with higher  
173 aerosol loading in Fog1 affects those in Fog2.

### 174 3 Simulation evaluation

175 Simulation evaluations for temperature, relative humidity, and wind speed are shown in Fig. 2.  
176 The correlation coefficients of 2 m temperature ( $T_{2m}$ ), 2 m relative humidity ( $RH_{2m}$ ), and 10 m  
177 wind speed ( $WS_{10m}$ ) between the simulations and observations are 0.9, 0.9, and 0.6, respectively,  
178 passing the significance test at 99%. Therefore, the simulations are generally consistent with  
179 the observations. The mean bias (MB) of  $T_{2m}$ ,  $RH_{2m}$ , and  $WS_{10m}$  between the simulations and  
180 observations are 1.0 °C, 2.7%, and 0.4 m s<sup>-1</sup>, respectively, consistent with evaluation results in  
181 studies by Hu et al. (2021), Gao et al. (2016), and Yang et al. (2022). Figure 3 shows the  
182 evaluation of  $PM_{2.5}$  distribution, and Table 2 summarises statistics of the mean mass  
183 concentration of  $PM_{2.5}$  based on the method proposed by Boylan and Russell (2006). The  
184 normalised mean bias (NMB), normalised mean error (NME), mean fractional bias (MFB), and  
185 mean fractional error (MFE) between the simulations and observations are 25%, 30%, 24%,  
186 and 28%, respectively (Eqs. S3–S6 in the supplement). Although the  $PM_{2.5}$  mass concentration  
187 is overestimated, it remains within a reasonable range (Shu et al., 2021; Yang et al., 2022; Zhai  
188 et al., 2018).

189 Figure 4 shows the evaluation of fog spatial distribution. The simulated fog optical depth  
190 distribution is compared with the Himawari-8 cloud optical depth products at 08:00 LST on 26  
191 and 27 November 2018, respectively. To identify observed fog at ground-based stations (the  
192 black circles in Fig. 4), we apply two criteria: visibility less than 1 km and relative humidity  
193 greater than 90% (Yan et al., 2020). Qualitatively, the value of fog optical depth and the fog  
194 spatial distribution in the simulation are roughly similar to those observed by the Himawari  
195 satellite and at ground-based stations. Likewise, Lee et al. (2016) evaluated fog distribution  
196 simulations against satellite-derived cloud optical depth from satellite and concluded that the  
197 distributions of simulations and observations were generally comparable to each other.



198 Further, to quantitatively evaluate the simulation, the Heidke skill score (HSS) is  
199 calculated as follows (Barnston, 1992):

$$200 \quad HSS = \frac{2(ad - bc)}{(a + c)(c + d) + (a + b)(b + d)} \quad (1)$$

201 Elements  $a-d$  are determined by the occurrence of fog at observation stations located in domain  
202 03 and the closest model grids to those observations, as shown in Table 3. If fog events are both  
203 observed at stations and simulated at the closest model grids, we recognize those as "hits" and  
204  $a$  in Eq.1 represents the total number of "hits" during the entire fog event. Similarly,  $d$  represents  
205 the number of "correct negatives" for the correct non-event simulations. On the other hand, if  
206 fog events are simulated but not observed, we recognize those as "false alarms" and  $b$  represents  
207 the total number of "false alarms" during the entire fog event. Conversely,  $c$  represents the total  
208 number of "misses", which indicates that fog events are observed but not simulated. The criteria  
209 of observed fog are shown in the last paragraph. Simulated foggy grids are classified based on  
210 three criteria (Jia et al., 2019; Zhao et al., 2013): fog water mixing ratio over  $0.01 \text{ g kg}^{-1}$ ,  $N_d$   
211 greater than  $1 \text{ cm}^{-3}$ , and fog base touching the ground. The perfect HSS score is 1.0, indicating  
212 that simulations are identical to observations. Here, the HSS score are 0.34 and 0.36 in Fog1  
213 and Fog2, respectively, which are close to previous reports (Mecikalski et al., 2008; Xu et al.,  
214 2020; Yamane et al., 2010). Therefore, the model generally captures the fog spatial distribution.

#### 215 **4 Larger aerosol-induced changes in Fog2 than in Fog1**

216 Here, we analyse the fog macro- and microphysical characteristics under clean and polluted  
217 conditions (Fig. 5). To ensure sufficient sample size for statistical analysis, only data with the  
218 fog area fraction larger than 5% are analysed. The fog area fraction is calculated as the number  
219 of foggy grid cells divided by the total number of grids in domain 03. We also test other

220 thresholds, 1%, 2.5%, 7.5%, and 10% (Fig. S3). The results are similar to those based on the  
221 threshold of 5%.

222 The ratios of changes between the polluted and clean conditions reveal that high aerosol  
223 loading affects fog macro- and microphysical properties in Fog1 and Fog2 (Fig. 5a). Compared  
224 to fog microphysics under clean conditions,  $N_d$  and LWC in Fog1 increase by respectively 463.0%  
225 and 81.7%; however,  $R_e$  decreased by 32.1% under polluted conditions. Furthermore, because  
226 of the ACI,  $N_d$  and LWC in Fog2 increase by respectively 672.4% and 113.5%; however  $R_e$   
227 decreases by 40.0%. Therefore, aerosol-induced changes in Fog2 are larger than those in Fog1,  
228 as shown in Fig. 5a ( $N_d$ : 209.5%, LWC: 31.8%, and  $R_e$ : -6.9%). Similarly, aerosol-induced  
229 changes in fog macrophysics are larger in Fog2. Compared with values under clean conditions,  
230 the fog area, fog-top height, and duration in Fog1 increase by respectively 23.1%, 109.6%, and  
231 20.0% under polluted conditions; the corresponding values in Fog2 are larger (34.9%, 350.5%,  
232 and 25.0%, respectively). In addition, LWP and fog optical depth ( $\tau_c$ ) exhibit similar trends.  
233 With a similar trend between observation and simulation, Figure S4 shows that aerosol mass  
234 concentration is similar before Fog1 and Fog2 formation, and aerosol number concentration  
235 before Fog2 is less than that before Fog1 formation. Therefore, changes in aerosol concentration  
236 are not the main reason for the increase in aerosol-induced changes in the two fog properties.  
237 To determine whether ACI under polluted conditions leads to an increase in aerosol-induced  
238 changes in Fog1 and Fog2, we design a sensitivity test called EXP3, as mentioned above.  
239 Furthermore, to quantitatively evaluate the strength of ACI in the two fog events, we examine  
240 the responses of  $\tau_c$  to changes in  $N_d$  (Eq. 2) (Ghan et al., 2016):

$$241 \quad \frac{\Delta \ln \tau_c}{\Delta \ln N_d} = \frac{\Delta \ln LWP}{\Delta \ln N_d} - \frac{\Delta \ln R_e}{\Delta \ln N_d} \quad (2)$$

242 Based on the similar aerosol concentration background (Fig. S4), the responses of  $\tau_c$  to  
243 changes in  $N_d$  quantitatively confirm which fog has stronger ACI. As shown in Table 4, the

244 strength of ACI in Fog2 (1.32) is larger than that in Fog1 (0.98). If Fog1 occurs under clean  
245 conditions and Fog2 occurs under polluted conditions (EXP3), ACI in Fog2 is 1.17, which is  
246 lower than that in EXP1 (1.32). This implies that high aerosol loading in Fog1 enhances ACI  
247 in Fog2. Relative changes in the above properties between Fog1 and Fog2 are calculated as  
248  $(\text{Fog2} - \text{Fog1})/\text{Fog1}$ . The values of  $\Delta \ln \tau_c / \Delta \ln N_d$ ,  $\Delta \ln LWP / \Delta \ln N_d$ , as well as  $-\Delta \ln R_e / \Delta \ln N_d$  are  
249 34.7%, 42.1%, and 9.1% larger in Fog2 than in Fog1, respectively. These numbers  
250 quantitatively confirm stronger ACI in Fog2 and indicate that LWP is the dominant factor for  
251 enhancing ACI. LWP depends on the fog-top height and LWC. As shown in Fig. 5a, when  
252 aerosol loading changes from clean to pollution, the rate of increase in fog-top height in Fog2  
253 (350.5%) is much larger than that in Fog1 (109.6%). Although the increase in LWC in Fog2  
254 (113.5%) is also larger than that in Fog1 (81.7%), the magnitude of increase in LWC is smaller  
255 than that increase in fog-top height, indicating that ACI are more sensitive to fog-top height  
256 than to LWC.

257 Fog duration is determined by the time of fog formation and dissipation, which is primarily  
258 extended because high aerosol loading delays fog dissipation, as reported previously (Jia et al.,  
259 2019; Quan et al., 2021). In this study, high aerosol loading not only delays fog dissipation but  
260 also promotes earlier fog formation, particularly during Fog2 (Fig. 5b). Fog formation is related  
261 to the PBL conditions which are affected by ACI. To investigate the aerosol effect on the Fog2  
262 formation stage, fog spatial distribution at the formation stage from 19:00 LST to 21:00 LST  
263 on 26 November is examined, as shown in Fig. 6. The fog area is rather small at 19:00 LST  
264 under both polluted and clean conditions. At 20:00 LST, fog formation is similar under both  
265 polluted and clean conditions in grid cells located outside the black box. However, inside the  
266 black box, there are several foggy grid cells under polluted conditions. At 21:00 LST, fog area  
267 in the black box further expands under polluted conditions. However, there is almost no fog in  
268 the black box at 20:00 and 21:00 LST under clean conditions. Therefore, high aerosol loading

269 promotes earlier formation of Fog2, which is primarily caused by meteorological conditions in  
270 the PBL inside the black box. In addition, the fog area outside the black box is larger under  
271 polluted conditions than under clean conditions, which is mainly related to the stronger  
272 turbulence diffusion under polluted conditions. A detailed analysis is presented in Sect. 5.

## 273 **5 Physical mechanisms underlying the larger aerosol-induced changes in Fog2 than in** 274 **Fog1**

### 275 **5.1. More conducive meteorological conditions to Fog2 formation**

276 Meteorological conditions in the PBL affect fog formation time and ACI during fog events. As  
277 shown in Table 5, under clean conditions,  $RH_{2m}$  before Fog2 formation is higher and PBL  
278 height (PBLH) is lower than those before Fog1 formation in domain 03. Polluted conditions  
279 yield similar results. Furthermore, compared with the difference in aerosol-induced changes in  
280  $RH_{2m}$  and PBLH before fog formation,  $RH_{2m}$  increases by 6% and PBLH decreases by 92 m  
281 under polluted conditions, which is larger than those ( $RH_{2m}$ : 4% and PBLH:  $-59$  m) under clean  
282 conditions. Therefore, high aerosol loading generates meteorological conditions more  
283 conducive to Fog2 formation during the two successive fog events.

284 To further analyse how high aerosol loading promotes Fog2 formation, we focus on the  
285 black box in Fig. 6, as described in Sect. 4 and by Yan et al. (2021). The regional average  
286 differences in the total optical depth ( $\tau_t$ ), downwelling short-wave radiation (SW) at the ground,  
287  $T_{2m}$ , PBLH,  $RH_{2m}$ , and water vapour mixing ratio ( $Q_{v_{bot}}$ ) at the model bottom layer (8 m) in  
288 the black box between polluted and clean conditions are calculated (Fig. 7). Compared with  
289 clean conditions, the larger  $\tau_t$  (mainly due to larger  $\tau_c$ ) and delayed fog dissipation in polluted  
290 conditions reduce short-wave radiation reaching the ground (from  $-46$  W m<sup>-2</sup> to  $-121$  W m<sup>-2</sup>)  
291 during the Fog1 dissipation time. This leads to a decrease in  $T_{2m}$  (from  $-0.2$  °C to  $-1$  °C) and

292 PBLH (from  $-42$  m to  $-118$  m), which further prolongs fog duration (Fig. 7). Notably,  $Q_{v_{bot}}$   
293 under polluted conditions is lower than that under clean conditions before the complete  
294 dissipation of Fog1, because of reduced fog water evaporation. When the fog dissipates  
295 completely, the lower PBLH accumulates more water vapour, increasing  $Q_{v_{bot}}$  and  $RH_{2m}$ . The  
296 positive feedbacks between ACI and PBL are similar to the feedbacks between high aerosol  
297 loading and the PBL reviewed by Li et al. (2017b). Furthermore, the feedback mechanism  
298 between high aerosol loading and PBL introduced by Zhong et al. (2018) supports the daytime  
299 feedbacks between fog and the PBL in the present study. Additionally, aerosol extinction is also  
300 considered in  $\tau$ . Whether aerosol optical depth (AOD) affects PBL significantly should also be  
301 discussed. As shown in Table 5,  $RH_{2m}$  and PBLH before Fog1 on 25 November under clean  
302 conditions are 76% and 669 m, respectively, similar to those under polluted conditions (76%  
303 and 670 m, respectively). Therefore, it is unlikely that aerosol–meteorology interaction leads to  
304 the meteorological differences in Fig. 7. In addition, a previous study (Yan et al., 2021) also  
305 noted that aerosol–fog interaction was more remarkable than aerosol–radiation interaction.  
306 Therefore, lower temperature, higher relative humidity, and higher stability result from ACI in  
307 Fog1 under polluted conditions, contributing to the earlier formation of Fog2.

308       Larger  $\tau_c$  and delayed dissipation result in lower temperature, higher relative humidity, and  
309 higher stability by affecting solar radiation during the daytime. How are these conducive  
310 conditions maintained after the sunset around 17:00 LST? Figure 8a shows that cold advection  
311 is the major reason for the difference in temperature between polluted and clean conditions. We  
312 further seek to unveil the reason why cold advection is stronger under polluted conditions.  
313 Figure 8b shows a cold centre, with wind diverging outwards. The cold centre is related to lower  
314 temperature under polluted conditions due to larger  $\tau_c$  and longer duration in Fog1. Likewise,  
315 Steeneveld and De Bode (2018) noted that fog appeared earlier with cold advection. In addition,

316 lower PBLH induced by high aerosol loading promote the maintenance of higher humidity and  
317 stability.

318 Overall, due to ACI at the Fog1 dissipation stage, the meteorological conditions are more  
319 conducive for promoting Fog2 formation. Furthermore, this interaction enhances the feedbacks  
320 in the fog physical processes, thus leading to a stronger ACI in Fog2. Details are discussed in  
321 Sect. 5.2 and 5.3.

322

## 323 **5.2. Feedbacks between microphysics and long-wave cooling**

324 Section 5.1 reveals the mechanism through which ACI in Fog1 leads to meteorological  
325 conditions more conducive to Fog2 formation. In Sect. 5.2, we demonstrate how conducive  
326 meteorological conditions play a fundamental role in promoting feedbacks between  
327 microphysics and long-wave cooling, resulting in a stronger ACI in Fog2.

328 As shown in Fig. 5a, aerosol-induced changes in  $N_d$  and LWC during Fog2 are larger than  
329 those during Fog1 because lower temperature and higher humidity are more conducive for  
330 aerosol activation and fog condensation (Petters and Kreidenweis, 2007; Simmel and Wurzler,  
331 2006). Owing to competition for available water vapour (Mazoyer et al., 2022; Yum and  
332 Hudson, 2005),  $R_e$  in Fog2 is smaller than that in Fog1. As shown in Fig. 9a, LWP is larger  
333 under polluted conditions than that under clean conditions, particularly for Fog2. The average  
334 LWP in Fog1 and Fog2 under polluted conditions are  $11.6 \text{ g m}^{-2}$  and  $24.3 \text{ g m}^{-2}$ , respectively.  
335 When LWP is less than  $20 \text{ g m}^{-2}$ , vertically integrated long-wave cooling and short-wave  
336 heating are stronger under polluted conditions than those under clean conditions (Fig. 9b). This  
337 is similar to the results from Petters et al. (2012) and Prabhakaran et al. (2023). Because  $N_d$   
338 shows a similar trend with LWP (Fig. S5), the dependence of heating and cooling rates on  
339 droplet concentration is consistent with the results based on LWP. Additionally, increased  $\tau_c$

340 in Fog2 triggers stronger positive feedbacks between microphysics and long-wave cooling,  
341 further enhancing cooling, activation, and condensation and thereby increasing  $N_d$  and LWC.  
342 Jia et al. (2019) emphasised that high aerosol loading promoted these positive feedbacks. This  
343 study further highlights the synergistic effects of high aerosol loading and meteorological  
344 conditions on the enhancement of positive feedbacks, which promotes ACI in Fog2.

345 To better understand how the above positive feedbacks affect ACI, Figure 10 presents the  
346 average extinction coefficient through the fog, that is,  $\tau_c$  at per unit height ( $\tau_c/\Delta h$ ), radiative  
347 cooling rate ( $T_{LW}$ ), condensational growth rate ( $LWC_{COND}$ ), and LWC tendency due to vertical  
348 mixing ( $LWC_{mixing}$ ) in the two successive fog events. Radiative cooling is the strongest near the  
349 fog top and weakest near the fog base (Ducongé et al., 2020; Mazoyer et al., 2017; Wærsted et  
350 al., 2017). Consequently,  $LWC_{COND}$  and  $LWC_{mixing}$  both follow similar profiles in response to  
351 radiative cooling. Therefore, if the vertical profiles of the three terms use absolute height, they  
352 will be distorted. To overcome this problem, physical quantities are normalised by the fog-top  
353 height. Compared with those in Fog1, larger extinction coefficient (Fig. 10a-b), stronger long-  
354 wave radiative cooling (Fig. 10c-d), and more condensation (Fig. 10e-f) near the fog top are  
355 noted in Fog2 because of the conducive conditions to Fog2 formation, which further increases  
356 LWC, fog-top height in Fog2 (black and purple lines) as well as LWP. Enhancement of these  
357 parameters indicate that the feedbacks between microphysics and long-wave cooling are  
358 stronger in Fog2 than in Fog1. As a result, ACI is stronger in Fog2 than in Fog1, due to  
359 favourable PBL conditions caused by ACI in Fog 1. In addition, as shown in Fig. 10g-h, vertical  
360 mixing transports fog water from the fog top to the fog base, and the strength of this  
361 transportation is stronger in Fog2 than in Fog1, because of stronger turbulent kinetic energy  
362 (TKE) in Fog2. The effect of TKE on fog is analysed in Sect. 5.3.

### 363 **5.3. Feedbacks between macrophysics, radiation, and turbulence**

364 Section 5.2 analyses the microphysics-related mechanisms underlying a stronger ACI in Fog2.  
365 This subsection not only focuses on macrophysics and its feedbacks with radiation and  
366 turbulence but also discusses how the combined effects of high aerosol loading and  
367 meteorological conditions impact the feedbacks and enhance ACI in Fog2, compared with those  
368 in Fog1. Briefly, fog macrophysics involves duration and distribution. The reason why the  
369 duration of Fog2 is longer than that of Fog1 is due to the earlier formation of Fog2, which is  
370 induced by meteorological conditions more conducive to Fog2 formation, as discussed in Sect.  
371 5.1. The reason for the wider distribution (fog-top height and fog area) is discussed here.

#### 372 **5.3.1 Effects of macrophysics on radiation**

373 Meteorological conditions more conducive to Fog2 formation and ACI promote condensation  
374 near the fog top (Fig. 10d, f), thereby raising the fog-top height in Fog2 compared with that in  
375 Fog1 (black and purple lines in Fig. 10). Therefore, both fog-top height and  $\tau_c$  in Fog2 are higher  
376 than those in Fog1. Compared with that in Fog1, the higher  $\tau_c$  in Fog2 enhances cooling near  
377 the fog top and downwelling long-wave radiation, weakening the cooling at the fog base than  
378 near the fog top (Fig. 10c). Additionally, the horizontal distribution of Fog2 is wider than that  
379 of Fog1 (Fig. 5b). Therefore, more foggy grid cells show more radiative cooling near the fog  
380 top and downwelling long-wave radiation at the fog base in Fog2.

#### 381 **5.3.2 Effects of radiation on turbulence**

382 The above analysis reveals the mechanism underlying the effects of meteorology and ACI on  
383 radiation in fog. How does radiation affect stability and turbulence (i.e., TKE)? To answer this  
384 question, we must know the dominant factors contributing to TKE, as described in the following  
385 TKE budget equation:



$$386 \quad \frac{\Delta TKE}{\Delta t} = TKE_{\text{shear}} + TKE_{\text{buoy}} - TKE_{\text{diss}} + TKE_{\text{mixing}} \quad (3)$$

387 where  $\Delta TKE/\Delta t$  is the TKE tendency with time (Fig. 11b), and the four terms on the right side  
 388 of Eq. (3) are contributors to TKE, including wind shear (Fig. 11c), buoyancy (Fig. 11d),  
 389 dissipation (Fig. 11e), and vertical mixing (Fig. 11f). Detailed equations of these contributions  
 390 to TKE are provided in supplementary information (Eqs. S7-S10) (Nakanishi and Niino (2009)).

391 As shown in Fig. 11a, TKE in Fog2 is stronger than that in Fog1, particularly under  
 392 polluted conditions. Since the vertical mixing term is one order smaller than the others, it is  
 393 negligible (Fig. 11f). At night, only the shear term is positive and, therefore, the main  
 394 contributor to TKE (Fig. 11c), consistent with the speculations of Kim and Yum (2012).  
 395 However, the dominant term driving the differences in TKE between polluted and clean  
 396 conditions is buoyancy (Fig. 11d). As shown in Fig. 11b,  $\Delta TKE/\Delta t$  is larger under polluted  
 397 conditions than under clean conditions. Meanwhile, the shear term is smaller but the buoyancy  
 398 term is larger under polluted conditions than under clean conditions, and the dissipation term is  
 399 similar between the two conditions. Therefore, the buoyancy term is the main factor that  
 400 increase TKE under polluted conditions, corroborating the qualitative speculations by Jia et al.  
 401 (2019). This is particularly true for Fog2. In addition, at daytime,  $\Delta TKE/\Delta t$  is weaker under  
 402 polluted conditions, because higher  $\tau_c$  reduces short-wave radiation reaching the surface. These  
 403 results are consistent with the higher stability during the dissipation stage under polluted  
 404 conditions, as described in Sect. 5.1.

405 After confirming the importance of the buoyancy term, we analyse the effect of radiation  
 406 on buoyancy and then on TKE. Buoyancy contributions to TKE are determined by temperature  
 407 inversion in the PBL at the night time. As shown in Fig. 12a-b, temperature inversion is close  
 408 to the surface. With the effect of ACI, much stronger radiative cooling leads to a more rapid  
 409 temperature drop at the fog top than at the fog base (Fig. 12c), thereby causing weaker

410 temperature inversion under polluted conditions. Therefore, stability is weaker and TKE is  
411 larger under polluted conditions, particularly in Fog2.

### 412 **5.3.3 Effects of turbulence on macrophysics**

413 Previous observations (Liu et al., 2010; Román-Cascón et al., 2016) and large eddy simulations  
414 (Bergot, 2013; Mazoyer et al., 2017; Nakanishi, 2000) showed that turbulence could increase  
415 the fog-top height. In this study, we note that increasing TKE increases fog-top height (black  
416 and purple lines in Fig. 10) and fog area (Fig. 5b), which is consistent with observations of Jia  
417 et al. (2019) and Quan et al. (2021). The increased fog-top height increases TKE by promoting  
418 radiative cooling near the fog top and weakening temperature inversion. This reflects the  
419 feedbacks between macrophysics, radiation, and turbulence. Overall, owing to meteorological  
420 conditions more conducive to Fog2 formation, the feedbacks are stronger in Fog2 than in Fog1.

## 421 **6 Conclusion**

422 To explore the interactions between the PBL and ACI, as well as their effects on fog properties,  
423 WRF-Chem 4.1.3 is used to simulate two successive radiation fog events that occurs in the  
424 northern YRD region in China on 26 and 27 November 2018. Two fog events simulation (Fog1  
425 and Fog2) well reproduces the observed results.

426 The results show higher LWC, higher  $N_d$ , smaller  $R_e$ , higher fog-top height, longer duration,  
427 wider spatial distribution, higher LWP, and higher  $\tau_c$  under polluted conditions than under clean  
428 conditions. Aerosol-induced changes in micro and macro-physical properties are more  
429 significant in Fog2 than in Fog1. When Fog1 occurs under clean conditions, the response of  
430 Fog2 to high aerosol loading becomes weaker. Therefore, ACI with high aerosol loading in  
431 Fog1 promotes aerosol-induced changes in Fog2. A conceptual diagram is proposed to describe

432 the mechanism of fog property changes as well as ACI evolution during two successive  
433 radiation fog events (Fig. 13). Moreover, the mechanisms of changes in fog properties and ACI  
434 evolution are discussed based on the synergistic effects of aerosols and meteorological  
435 conditions. The microphysics–radiation feedbacks and macrophysics–radiation–turbulence  
436 feedbacks delay Fog1 dissipation, generating more conducive conditions for promoting the  
437 earlier formation of Fog2. Furthermore, the microphysics–radiation feedbacks and  
438 macrophysics–radiation–turbulence feedbacks are strengthened in Fog2 due to the conditions  
439 more conducive to Fog2 formation, enhancing ACI in Fog2 compared with those in Fog1.  
440 Detailed mechanisms are summarised below, including meteorological conditions and the two  
441 types of feedbacks.

442 First, meteorological conditions before Fog2 formation are more conducive than those  
443 before Fog1 formation, which play fundamental roles in changing fog properties and enhancing  
444 ACI during two fog events. This is related to the delayed dissipation of Fog1 induced by  $\tau_c$ .  
445 During Fog1 dissipation (daytime), the cooling effect caused by the higher  $\tau_c$  contributes to the  
446 lower temperature, higher relative humidity, and higher stability. At night, cold advection near  
447 the ground is enhanced. Meanwhile, the temperature remains low, forming a cold centre, due  
448 to low daytime temperature. Moreover, the surface wind diverges outward from the cold centre,  
449 strengthening the cold advection. Ultimately, the meteorological conditions induced by high  
450 aerosol loading are more conducive for promoting the earlier formation as well as a longer  
451 duration of Fog2 than of Fog1.

452 Second, the positive feedbacks between microphysics and radiative cooling are crucial  
453 physical mechanisms for changing fog properties and enhancing ACI. In Fog2, high aerosol  
454 loading and more conducive meteorological conditions synergistically promote fog  
455 microphysics. Lower temperature and higher relative humidity promote aerosol activation and  
456 condensation. Consequently,  $N_d$ , LWP, and  $\tau_c$  are higher, whereas  $R_e$  is smaller, in Fog2 than in

457 Fog1. Radiative cooling and heating within the fog layer depend on LWP and  $N_d$ . When LWP  
458 in fog is less than  $20 \text{ g m}^{-2}$ , and higher aerosol loading enhances vertically integrated cooling  
459 and heating in optically thin fog. These variations in microphysics lead to stronger long-wave  
460 radiative cooling and condensational growth near the top of Fog2. Therefore, the positive  
461 feedbacks between microphysics and radiation are stronger in Fog2, which further promote  
462 stronger ACI.

463 Finally, the feedbacks between fog macrophysics, radiation, and turbulence affect fog  
464 properties. Under polluted conditions, the higher fog top strengthens the fog-top long-wave  
465 radiative cooling and then reduces the strength of temperature inversion near the surface and  
466 enhances turbulence. Stronger turbulence further increases the fog-top height and fog area.  
467 Because of meteorological conditions more conducive to Fog2 formation, the feedbacks are  
468 stronger in Fog2 than in Fog1, contributing to the enhancement of ACI.

469 This study focuses on a two-day radiation fog event in the Yangtze River Delta, China,  
470 which has a large population. The conclusions are expected to be applicable to radiation fog  
471 events in this region and other regions with similar human activities. It would be interesting to  
472 see if similar conclusions can be found in other fog types (e.g., advection fog) in other regions  
473 (e.g., ocean). Furthermore, there are large uncertainties in the aerosol–cloud interaction (Fan et  
474 al., 2016; Guo et al., 2018; Rosenfeld et al., 2019; Seinfeld et al., 2016; Zhu and Penner, 2020;  
475 Zhu et al., 2019). The findings of our study offer novel insights into the potential involvement  
476 of mechanisms responsible for evolution of ACI, particularly for stratus, which is similar to fog.

477 Data and code availability. The data repositories have been listed in Sect. 2. Codes are accessed  
478 by contacting Chunsong Lu via [luchunsong110@gmail.com](mailto:luchunsong110@gmail.com).

479

480 Author contributions. NS performed the data analysis, model simulation, and article writing.  
481 CL proposed the idea, supervised the work, and revised the article. XJ and YW both took part

482 in revising the article and gave suggestions. Ground-based observation data were provided by  
483 XJ and DL. YL supervised the analysis of the turbulence kinetic energy budget. TZ supported  
484 the work that anthropogenic emissions were driven by Multiresolution Emission Inventory for  
485 China (MECI). SN provided financial support. NS prepared the article with help from YY, BZ,  
486 SF, SY, and JL.

487

488 Competing interests. The authors in this article declare that they have no conflict of interest  
489 with others.

490

491 Acknowledgements. This Article is supported by the National Key Scientific and  
492 Technological Infrastructure project “Earth System Science Numerical Simulator Facility”  
493 (EarthLab), and we acknowledge the High Performance Computing Centre of Nanjing  
494 University of Information Science & Technology for their support of this work.

495

496 Financial support. This research has been supported by the National Natural Science  
497 Foundation of China (grant nos. 42027804, 41775134, 41975181, 42205072) and the Science  
498 and Technology Planning Project of Gansu Province (grant no. 22JR5RA445).

499

## 500 **References**

501 Abdul-Razzak, H.: A parameterization of aerosol activation 3. Sectional representation, J.  
502 Geophys. Res., 107, <https://doi.org/10.1029/2001jd000483>, 2002.

503 Ackerman, A. S., Kirkpatrick, M. P., Stevens, D. E., and Toon, O. B.: The impact of humidity  
504 above stratiform clouds on indirect aerosol climate forcing, Nature, 432, 1014-1017,  
505 <https://doi.org/10.1038/nature03174>, 2004.

506 Barnston, A. G.: Correspondence among the Correlation, RMSE, and Heidke Forecast  
507 Verification Measures; Refinement of the Heidke Score, *Weather Forecasting*, 7, 699-709,  
508 [https://doi.org/10.1175/1520-0434\(1992\)007<0699:catcra>2.0.co;2](https://doi.org/10.1175/1520-0434(1992)007<0699:catcra>2.0.co;2), 1992.

509 Bessho, K., Date, K., Hayashi, M., Ikeda, A., Imai, T., Inoue, H., Kumagai, Y., Miyakawa, T.,  
510 Murata, H., and Ohno, T.: An introduction to Himawari-8/9—Japan’s new-generation  
511 geostationary meteorological satellites, *Journal of the Meteorological Society of Japan. Ser.*  
512 *II*, 94, 151-183, <https://doi.org/10.2151/jmsj.2016-009>, 2016.

513 Boutle, I., Price, J., Kudzotsa, I., Kokkola, H., and Romakkaniemi, S.: Aerosol–fog interaction  
514 and the transition to well-mixed radiation fog, *Atmos. Chem. Phys.*, 18, 7827-7840,  
515 <https://doi.org/10.5194/acp-18-7827-2018>, 2018.

516 Boylan, J. W. and Russell, A. G.: PM and light extinction model performance metrics, goals,  
517 and criteria for three-dimensional air quality models, *Atmos. Environ.*, 40, 4946-4959,  
518 <https://doi.org/10.1016/j.atmosenv.2005.09.087>, 2006.

519 Chaboureaud, J.-P. and Bechtold, P.: A Simple Cloud Parameterization Derived from Cloud  
520 Resolving Model Data: Diagnostic and Prognostic Applications, *J. Atmos. Sci.*, 59, 2362-  
521 2372, [https://doi.org/10.1175/1520-0469\(2002\)059<2362:ascpdf>2.0.co;2](https://doi.org/10.1175/1520-0469(2002)059<2362:ascpdf>2.0.co;2), 2002.

522 Ding, Q., Sun, J., Huang, X., Ding, A., Zou, J., Yang, X., and Fu, C.: Impacts of black carbon  
523 on the formation of advection–radiation fog during a haze pollution episode in eastern China,  
524 *Atmos. Chem. Phys.*, 19, 7759-7774, <https://doi.org/10.5194/acp-19-7759-2019>, 2019.

525 Ducongé, L., Lac, C., Vié, B., Bergot, T., and Price, J. D.: Fog in heterogeneous environments:  
526 the relative importance of local and non-local processes on radiative-advective fog formation,  
527 *Q. J. R. Meteorolog. Soc.*, 146, 2522-2546, <https://doi.org/10.1002/qj.3783>, 2020.

528 Fernando, H. J. S., Gultepe, I., Dorman, C., Pardyjak, E., Wang, Q., Hoch, S. W., Richter, D.,  
529 Creegan, E., Gaberšek, S., Bullock, T., Hocut, C., Chang, R., Alappattu, D., Dimitrova, R.,  
530 Flagg, D., Grachev, A., Krishnamurthy, R., Singh, D. K., Lozovatsky, I., Nagare, B., Sharma,  
531 A., Wagh, S., Wainwright, C., Wroblewski, M., Yamaguchi, R., Bardoel, S., Coppersmith,

532 R. S., Chisholm, N., Gonzalez, E., Gunawardena, N., Hyde, O., Morrison, T., Olson, A.,  
533 Perelet, A., Perrie, W., Wang, S., and Wauer, B.: C-FOG: Life of Coastal Fog, *Bull. Am.*  
534 *Meteorol. Soc.*, 102, E244-E272, <https://doi.org/10.1175/bams-d-19-0070.1>, 2021.

535 Fitzjarrald, D. R. and Lala, G. G.: Hudson Valley Fog Environments, *J. Appl. Meteorol. Clim.*,  
536 28, 1303-1328, [https://doi.org/10.1175/1520-0450\(1989\)028<1303:hvfe>2.0.co;2](https://doi.org/10.1175/1520-0450(1989)028<1303:hvfe>2.0.co;2), 1989.

537 Gao, M., Carmichael, G. R., Wang, Y., Saide, P. E., Yu, M., Xin, J., Liu, Z., and Wang, Z.:  
538 Modeling study of the 2010 regional haze event in the North China Plain, *Atmos. Chem.*  
539 *Phys.*, 16, 1673-1691, <https://doi.org/10.5194/acp-16-1673-2016>, 2016.

540 Garrett, T. J. and Zhao, C.: Increased Arctic cloud longwave emissivity associated with  
541 pollution from mid-latitudes, *Nature*, 440, 787-789, <https://doi.org/10.1038/nature04636>,  
542 2006.

543 Ghan, S., Wang, M., Zhang, S., Ferrachat, S., Gettelman, A., Griesfeller, J., Kipling, Z.,  
544 Lohmann, U., Morrison, H., and Neubauer, D.: Challenges in constraining anthropogenic  
545 aerosol effects on cloud radiative forcing using present-day spatiotemporal variability, *Proc.*  
546 *Natl. Acad. Sci. U.S.A.*, 113, 5804-5811, <https://doi.org/10.1073/pnas.1514036113>, 2016.

547 Grell, G. A. and Dévényi, D.: A generalized approach to parameterizing convection combining  
548 ensemble and data assimilation techniques, *Geophys. Res. Lett.*, 29, 38-31-38-34,  
549 <https://doi.org/10.1029/2002gl015311>, 2002.

550 Gultepe, I., Kuhn, T., Pavolonis, M., Calvert, C., Gurka, J., Heymsfield, A. J., Liu, P. S. K.,  
551 Zhou, B., Ware, R., Ferrier, B., Milbrandt, J., and Bernstein, B.: Ice Fog in Arctic During  
552 FRAM–Ice Fog Project: Aviation and Nowcasting Applications, *Bull. Am. Meteorol. Soc.*,  
553 95, 211-226, <https://doi.org/10.1175/bams-d-11-00071.1>, 2014.

554 Guo, L., Guo, X., Fang, C., and Zhu, S.: Observation analysis on characteristics of formation,  
555 evolution and transition of a long-lasting severe fog and haze episode in North China, *Sci.*  
556 *China, Ser. D Earth Sci.*, 58, 329-344, <https://doi.org/10.1007/s11430-014-4924-2>, 2015.

557 Guo, L., Guo, X., Luan, T., Zhu, S., and Lyu, K.: Radiative effects of clouds and fog on long-  
558 lasting heavy fog events in northern China, *Atmos. Res.*, 252, 105444,  
559 <https://doi.org/10.1016/j.atmosres.2020.105444>, 2021.

560 Haeffelin, M., Bergot, T., Elias, T., Tardif, R., Carrer, D., Chazette, P., Colomb, M., Drobinski,  
561 P., Dupont, E., Dupont, J.-C., Gomes, L., Musson-Genon, L., Pietras, C., Plana-Fattori, A.,  
562 Protat, A., Rangognio, J., Raut, J.-C., Rémy, S., Richard, D., Sciare, J., and Zhang, X.:  
563 Parisfog: Shedding new Light on Fog Physical Processes, *Bull. Am. Meteorol. Soc.*, 91, 767-  
564 783, <https://doi.org/10.1175/2009bams2671.1>, 2010.

565 Hammer, E., Gysel, M., Roberts, G. C., Elias, T., Hofer, J., Hoyle, C. R., Bukowiecki, N.,  
566 Dupont, J. C., Burnet, F., Baltensperger, U., and Weingartner, E.: Size-dependent particle  
567 activation properties in fog during the ParisFog 2012/13 field campaign, *Atmos. Chem.*  
568 *Phys.*, 14, 10517-10533, <https://doi.org/10.5194/acp-14-10517-2014>, 2014.

569 Holets, S. and Swanson, R. N.: High-Inversion Fog Episodes in Central California, *J. Appl.*  
570 *Meteorol. Clim.*, 20, 890-899, [https://doi.org/10.1175/1520-0450\(1981\)020<0890:hifeic>2.0.co;2](https://doi.org/10.1175/1520-0450(1981)020<0890:hifeic>2.0.co;2), 1981.

572 Hu, W., Zhao, T., Bai, Y., Kong, S., Xiong, J., Sun, X., Yang, Q., Gu, Y., and Lu, H.:  
573 Importance of regional PM<sub>2.5</sub> transport and precipitation washout in heavy air pollution in  
574 the Twain-Hu Basin over Central China: Observational analysis and WRF-Chem simulation,  
575 *Sci. Total Environ.*, 758, 143710, <https://doi.org/10.1016/j.scitotenv.2020.143710>, 2021.

576 Iacono, M. J., Delamere, J. S., Mlawer, E. J., Shephard, M. W., Clough, S. A., and Collins, W.  
577 D.: Radiative forcing by long-lived greenhouse gases: Calculations with the AER radiative  
578 transfer models, *J. Geophys. Res.*, 113, <https://doi.org/10.1029/2008jd009944>, 2008.

579 Iwabuchi, H., Putri, N. S., Saito, M., Tokoro, Y., Sekiguchi, M., Yang, P., and Baum, B. A.:  
580 Cloud property retrieval from multiband infrared measurements by Himawari-8, *Journal of*  
581 *the Meteorological Society of Japan. Ser. II*, <https://doi.org/10.2151/jmsj.2018-001>, 2018.



582 Jia, X., Quan, J., Zheng, Z., Liu, X., Liu, Q., He, H., and Liu, Y.: Impacts of Anthropogenic  
583 Aerosols on Fog in North China Plain, *J. Geophys. Res.: Atmos.*, 124, 252-265,  
584 <https://doi.org/10.1029/2018jd029437>, 2019.

585 Kim, C. K. and Yum, S. S.: Local meteorological and synoptic characteristics of fogs formed  
586 over Incheon international airport in the west coast of Korea, *Adv. Atmos. Sci.*, 27, 761-776,  
587 <https://doi.org/10.1007/s00376-009-9090-7>, 2010.

588 Kim, C. K. and Yum, S. S.: A numerical study of sea-fog formation over cold sea surface using  
589 a one-dimensional turbulence model coupled with the weather research and forecasting  
590 model, *Boundary Layer Meteorol.*, 143, 481-505, [https://doi.org/10.1007/s10546-012-9706-](https://doi.org/10.1007/s10546-012-9706-9)  
591 [9](https://doi.org/10.1007/s10546-012-9706-9), 2012.

592 Kim, C. K. and Yum, S. S.: A study on the transition mechanism of a stratus cloud into a warm  
593 sea fog using a single column model PAFOG coupled with WRF, *Asia-Pac. J. Atmos. Sci.*,  
594 49, 245-257, <https://doi.org/10.1007/s13143-013-0024-z>, 2013.

595 Kumar, B., Bera, S., Prabha, T. V., and Grabowski, W. W.: Cloud-edge mixing: Direct  
596 numerical simulation and observations in Indian Monsoon clouds, *J. Adv. Model. Earth Syst.*,  
597 9, 332-353, <https://doi.org/10.1002/2016ms000731>, 2017.

598 Kumar, B., Ranjan, R., Yau, M.-K., Bera, S., and Rao, S. A.: Impact of high- and low-vorticity  
599 turbulence on cloud–environment mixing and cloud microphysics processes, *Atmos. Chem.*  
600 *Phys.*, 21, 12317-12329, <https://doi.org/10.5194/acp-21-12317-2021>, 2021.

601 Lee, H.-H., Chen, S.-H., Kleeman, M. J., Zhang, H., DeNero, S. P., and Joe, D. K.:  
602 Implementation of warm-cloud processes in a source-oriented WRF/Chem model to study  
603 the effect of aerosol mixing state on fog formation in the Central Valley of California, *Atmos.*  
604 *Chem. Phys.*, 16, 8353-8374, <https://doi.org/10.5194/acp-16-8353-2016>, 2016.

605 Letu, H., Yang, K., Nakajima, T. Y., Ishimoto, H., Nagao, T. M., Riedi, J., Baran, A. J., Ma,  
606 R., Wang, T., and Shang, H.: High-resolution retrieval of cloud microphysical properties and

607 surface solar radiation using Himawari-8/AHI next-generation geostationary satellite,  
608 Remote Sens. Environ., 239, 111583, <https://doi.org/10.1016/j.rse.2019.111583>, 2020.

609 Li, M., Liu, H., Geng, G., Hong, C., Liu, F., Song, Y., Tong, D., Zheng, B., Cui, H., Man, H.,  
610 Zhang, Q., and He, K.: Anthropogenic emission inventories in China: a review, Natl. Sci.  
611 Rev., 4, 834-866, <https://doi.org/10.1093/nsr/nwx150>, 2017a.

612 Li, Z., Guo, J., Ding, A., Liao, H., Liu, J., Sun, Y., Wang, T., Xue, H., Zhang, H., and Zhu, B.:  
613 Aerosol and boundary-layer interactions and impact on air quality, Natl. Sci. Rev., 4, 810-  
614 833, <https://doi.org/10.1093/nsr/nwx117>, 2017b.

615 Liu, D. Y., Niu, S. J., Yang, J., Zhao, L. J., Lü, J. J., and Lu, C. S.: Summary of a 4-Year Fog  
616 Field Study in Northern Nanjing, Part 1: Fog Boundary Layer, Pure Appl. Geophys., 169,  
617 809-819, <https://doi.org/10.1007/s00024-011-0343-x>, 2011.

618 Liu, Y., Hua, S., Jia, R., and Huang, J.: Effect of Aerosols on the Ice Cloud Properties Over the  
619 Tibetan Plateau, J. Geophys. Res.: Atmos., 124, 9594-9608,  
620 <https://doi.org/10.1029/2019jd030463>, 2019.

621 Liu, Y., Zhu, Q., Hua, S., Alam, K., Dai, T., and Cheng, Y.: Tibetan Plateau driven impact of  
622 Taklimakan dust on northern rainfall, Atmos. Environ., 234, 117583,  
623 <https://doi.org/10.1016/j.atmosenv.2020.117583>, 2020.

624 Maalick, Z., Kühn, T., Korhonen, H., Kokkola, H., Laaksonen, A., and Romakkaniemi, S.:  
625 Effect of aerosol concentration and absorbing aerosol on the radiation fog life cycle, Atmos.  
626 Environ., 133, 26-33, <https://doi.org/10.1016/j.atmosenv.2016.03.018>, 2016.

627 Maronga, B. and Bosveld, F. C.: Key parameters for the life cycle of nocturnal radiation fog: a  
628 comprehensive large-eddy simulation study, Q. J. R. Meteorolog. Soc., 143, 2463-2480,  
629 <https://doi.org/10.1002/qj.3100>, 2017.

630 Matsui, T., Zhang, S. Q., Lang, S. E., Tao, W.-K., Ichoku, C., and Peters-Lidard, C. D.: Impact  
631 of radiation frequency, precipitation radiative forcing, and radiation column aggregation on

632 convection-permitting West African monsoon simulations, *Clim. Dyn.*, 55, 193-213,  
633 <https://doi.org/10.1007/s00382-018-4187-2>, 2020.

634 Mazoyer, M., Burnet, F., and Denjean, C.: Experimental study on the evolution of droplet size  
635 distribution during the fog life cycle, *Atmos. Chem. Phys.*, 22, 11305-11321,  
636 <https://doi.org/10.5194/acp-22-11305-2022>, 2022.

637 Mazoyer, M., Lac, C., Thouron, O., Bergot, T., Masson, V., and Musson-Genon, L.: Large eddy  
638 simulation of radiation fog: impact of dynamics on the fog life cycle, *Atmos. Chem. Phys.*,  
639 17, 13017-13035, <https://doi.org/10.5194/acp-17-13017-2017>, 2017.

640 Mazoyer, M., Burnet, F., Denjean, C., Roberts, G. C., Haeffelin, M., Dupont, J.-C., and Elias,  
641 T.: Experimental study of the aerosol impact on fog microphysics, *Atmos. Chem. Phys.*, 19,  
642 4323-4344, <https://doi.org/10.5194/acp-19-4323-2019>, 2019.

643 Mecikalski, J. R., Bedka, K. M., Paech, S. J., and Litten, L. A.: A Statistical Evaluation of  
644 GOES Cloud-Top Properties for Nowcasting Convective Initiation, *Mon. Weather Rev.*, 136,  
645 4899-4914, <https://doi.org/10.1175/2008mwr2352.1>, 2008.

646 Morrison, H., Curry, J., and Khvorostyanov, V.: A new double-moment microphysics  
647 parameterization for application in cloud and climate models. Part I: Description, *J. Atmos.*  
648 *Sci.*, 62, 1665-1677, <https://doi.org/10.1175/JAS3446.1>, 2005.

649 Nakanishi, M. and Niino, H.: Development of an Improved Turbulence Closure Model for the  
650 Atmospheric Boundary Layer, *J. Meteorolog. Soc. Jpn.*, 87, 895-912,  
651 <https://doi.org/10.2151/jmsj.87.895>, 2009.

652 Niu, S., Lu, C., Yu, H., Zhao, L., and Lü, J.: Fog research in China: An overview, *Adv. Atmos.*  
653 *Sci.*, 27, 639-662, <https://doi.org/10.1007/s00376-009-8174-8>, 2010.

654 Niu, S. J., Liu, D. Y., Zhao, L. J., Lu, C. S., Lü, J. J., and Yang, J.: Summary of a 4-Year Fog  
655 Field Study in Northern Nanjing, Part 2: Fog Microphysics, *Pure Appl. Geophys.*, 169, 1137-  
656 1155, <https://doi.org/10.1007/s00024-011-0344-9>, 2011.

657 Petters, J. L., Harrington, J. Y., and Clothiaux, E. E.: Radiative–dynamical feedbacks in low  
658 liquid water path stratiform clouds, *J. Atmos. Sci.*, 69, 1498-1512,  
659 <https://doi.org/10.1175/JAS-D-11-0169.1>, 2012.

660 Petters, M. D. and Kreidenweis, S. M.: A single parameter representation of hygroscopic  
661 growth and cloud condensation nucleus activity, *Atmos. Chem. Phys.*, 7, 1961-1971,  
662 <https://doi.org/10.5194/acp-7-1961-2007>, 2007.

663 Porson, A., Price, J., Lock, A., and Clark, P.: Radiation Fog. Part II: Large-Eddy Simulations  
664 in Very Stable Conditions, *Boundary Layer Meteorol.*, 139, 193-224,  
665 <https://doi.org/10.1007/s10546-010-9579-8>, 2011.

666 Prabhakaran, P., Hoffmann, F., and Feingold, G.: Evaluation of Pulse Aerosol Forcing on  
667 Marine Stratocumulus Clouds in the Context of Marine Cloud Brightening, *J. Atmos. Sci.*,  
668 80, 1585-1604, <https://doi.org/10.1175/JAS-D-22-0207.1>, 2023.

669 Price, J. D., Lane, S., Boutle, I. A., Smith, D. K. E., Bergot, T., Lac, C., Duconge, L., McGregor,  
670 J., Kerr-Munslow, A., Pickering, M., and Clark, R.: LANFEX: A Field and Modeling Study  
671 to Improve Our Understanding and Forecasting of Radiation Fog, *Bull. Am. Meteorol. Soc.*,  
672 99, 2061-2077, <https://doi.org/10.1175/bams-d-16-0299.1>, 2018.

673 Quan, J., Zhang, Q., He, H., Liu, J., Huang, M., and Jin, H.: Analysis of the formation of fog  
674 and haze in North China Plain (NCP), *Atmos. Chem. Phys.*, 11, 8205-8214,  
675 <https://doi.org/10.5194/acp-11-8205-2011>, 2011.

676 Quan, J., Liu, Y., Jia, X., Liu, L., Dou, Y., Xin, J., and Seinfeld, J. H.: Anthropogenic aerosols  
677 prolong fog lifetime in China, *Environ. Res. Lett.*, 16, 044048, <https://doi.org/10.1088/1748-9326/abef32>, 2021.

679 Roach, W., Brown, R., Caughey, S., Garland, J., and Readings, C.: The physics of radiation fog:  
680 I—a field study, *Q. J. R. Meteorolog. Soc.*, 102, 313-333,  
681 <https://doi.org/10.1002/qj.49710243204>, 1976.

682 Shen, C., Zhao, C., Ma, N., Tao, J., Zhao, G., Yu, Y., and Kuang, Y.: Method to Estimate Water  
683 Vapor Supersaturation in the Ambient Activation Process Using Aerosol and Droplet  
684 Measurement Data, *J. Geophys. Res.: Atmos.*, 123, <https://doi.org/10.1029/2018jd028315>,  
685 2018.

686 Simmel, M. and Wurzler, S.: Condensation and activation in sectional cloud microphysical  
687 models, *Atmos. Res.*, 80, 218-236, <https://doi.org/10.1016/j.atmosres.2005.08.002>, 2006.

688 Steeneveld, G. J. and de Bode, M.: Unravelling the relative roles of physical processes in  
689 modelling the life cycle of a warm radiation fog, *Q. J. R. Meteorolog. Soc.*, 144, 1539-1554,  
690 <https://doi.org/10.1002/qj.3300>, 2018.

691 Stolaki, S., Haeffelin, M., Lac, C., Dupont, J. C., Elias, T., and Masson, V.: Influence of  
692 aerosols on the life cycle of a radiation fog event. A numerical and observational study,  
693 *Atmos. Res.*, 151, 146-161, <https://doi.org/10.1016/j.atmosres.2014.04.013>, 2015.

694 Toll, V., Christensen, M., Quaas, J., and Bellouin, N.: Weak average liquid-cloud-water  
695 response to anthropogenic aerosols, *Nature*, 572, 51-55, [https://doi.org/10.1038/s41586-  
696 019-1423-9](https://doi.org/10.1038/s41586-019-1423-9), 2019.

697 Twomey, S.: The influence of pollution on the shortwave albedo of clouds, *J. Atmos. Sci.*, 34,  
698 1149-1152, [https://doi.org/10.1175/1520-0469\(1977\)034<1149:TIOPOT>2.0.CO;2](https://doi.org/10.1175/1520-0469(1977)034<1149:TIOPOT>2.0.CO;2), 1977.

699 Vautard, R., Yiou, P., and van Oldenborgh, G. J.: Decline of fog, mist and haze in Europe over  
700 the past 30 years, *Nat. Geosci.*, 2, 115-119, <https://doi.org/10.1038/ngeo414>, 2009.

701 Wærsted, E. G., Haeffelin, M., Dupont, J.-C., Delanoë, J., and Dubuisson, P.: Radiation in fog:  
702 quantification of the impact on fog liquid water based on ground-based remote sensing,  
703 *Atmos. Chem. Phys.*, 17, 10811-10835, <https://doi.org/10.5194/acp-17-10811-2017>, 2017.

704 Wang, Y., Fan, J., Zhang, R., Leung, L. R., and Franklin, C.: Improving bulk microphysics  
705 parameterizations in simulations of aerosol effects, *J. Geophys. Res.: Atmos.*, 118, 5361-  
706 5379, <https://doi.org/10.1002/jgrd.50432>, 2013.

707 Wang, Y., Lu, C., Niu, S., Lv, J., Jia, X., Xu, X., Xue, Y., Zhu, L., and Yan, S.: Diverse  
708 dispersion effects and parameterization of relative dispersion in urban fog in eastern China,  
709 J. Geophys. Res.: Atmos., n/a, e2022JD037514, <https://doi.org/10.1029/2022JD037514>,  
710 2023.

711 Wang, Y., Vogel, J. M., Lin, Y., Pan, B., Hu, J., Liu, Y., Dong, X., Jiang, J. H., Yung, Y. L.,  
712 and Zhang, R.: Aerosol microphysical and radiative effects on continental cloud ensembles,  
713 Adv. Atmos. Sci., 35, 234-247, <https://doi.org/10.1007/s00376-017-7091-5>, 2018.

714 Wang, Y., Niu, S., Lu, C., Lv, J., Zhang, J., Zhang, H., Zhang, S., Shao, N., Sun, W., Jin, Y.,  
715 and Song, Q.: Observational study of the physical and chemical characteristics of the winter  
716 radiation fog in the tropical rainforest in Xishuangbanna, China, Sci. China, Ser. D Earth  
717 Sci., 64, 1982-1995, <https://doi.org/10.1007/s11430-020-9766-4>, 2021.

718 WMO: International meteorological vocabulary, WMO-182, 784 pp., 1992.

719 Xu, X., Lu, C., Liu, Y., Gao, W., Wang, Y., Cheng, Y., Luo, S., and Van Weverberg, K.: Effects  
720 of Cloud Liquid-Phase Microphysical Processes in Mixed-Phase Cumuli Over the Tibetan  
721 Plateau, J. Geophys. Res.: Atmos., 125, <https://doi.org/10.1029/2020jd033371>, 2020.

722 Yamane, Y., Hayashi, T., Dewan, A. M., and Akter, F.: Severe local convective storms in  
723 Bangladesh: Part II, Atmos. Res., 95, 407-418,  
724 <https://doi.org/10.1016/j.atmosres.2009.11.003>, 2010.

725 Yan, S., Zhu, B., Huang, Y., Zhu, J., Kang, H., Lu, C., and Zhu, T.: To what extents do  
726 urbanization and air pollution affect fog?, Atmos. Chem. Phys., 20, 5559-5572,  
727 <https://doi.org/10.5194/acp-20-5559-2020>, 2020.

728 Yan, S., Zhu, B., Zhu, T., Shi, C., Liu, D., Kang, H., Lu, W., and Lu, C.: The Effect of Aerosols  
729 on Fog Lifetime: Observational Evidence and Model Simulations, Geophys. Res. Lett., 48,  
730 <https://doi.org/10.1029/2020gl091156>, 2021.

731 Yang, Q., Zhao, T., Tian, Z., Kumar, K. R., Chang, J., Hu, W., Shu, Z., and Hu, J.: The Cross-  
732 Border Transport of PM<sub>2.5</sub> from the Southeast Asian Biomass Burning Emissions and Its

733 Impact on Air Pollution in Yunnan Plateau, Southwest China, *Remote Sens.*, 14, 1886,  
734 <https://doi.org/10.3390/rs14081886>, 2022.

735 Yang, Y., Zhao, C., and Fan, H.: Spatiotemporal distributions of cloud properties over China  
736 based on Himawari-8 advanced Himawari imager data, *Atmos. Res.*, 240, 104927,  
737 <https://doi.org/10.1016/j.atmosres.2020.104927>, 2020.

738 Yang, Y., Hu, X.-M., Gao, S., and Wang, Y.: Sensitivity of WRF simulations with the YSU  
739 PBL scheme to the lowest model level height for a sea fog event over the Yellow Sea, *Atmos.*  
740 *Res.*, 215, 253-267, <https://doi.org/10.1016/j.atmosres.2018.09.004>, 2019.

741 Ye, X., Wu, B., and Zhang, H.: The turbulent structure and transport in fog layers observed  
742 over the Tianjin area, *Atmos. Res.*, 153, 217-234,  
743 <https://doi.org/10.1016/j.atmosres.2014.08.003>, 2015.

744 Yum, S. S. and Hudson, J. G.: Adiabatic predictions and observations of cloud droplet spectral  
745 broadness, *Atmos. Res.*, 73, 203-223, <https://doi.org/10.1016/j.atmosres.2004.10.006>, 2005.

746 Zaveri, R. A. and Peters, L. K.: A new lumped structure photochemical mechanism for large-  
747 scale applications, *J. Geophys. Res.: Atmos.*, 104, 30387-30415,  
748 <https://doi.org/10.1029/1999jd900876>, 1999.

749 Zaveri, R. A., Easter, R. C., Fast, J. D., and Peters, L. K.: Model for Simulating Aerosol  
750 Interactions and Chemistry (MOSAIC), *J. Geophys. Res.*, 113,  
751 <https://doi.org/10.1029/2007jd008782>, 2008.

752 Zhao, C. and Garrett, T. J.: Effects of Arctic haze on surface cloud radiative forcing, *Geophys.*  
753 *Res. Lett.*, 42, 557-564, <https://doi.org/10.1002/2014gl062015>, 2015.

754 Zhao, L., Niu, S., Zhang, Y., and Xu, F.: Microphysical characteristics of sea fog over the east  
755 coast of Leizhou Peninsula, China, *Adv. Atmos. Sci.*, 30, 1154-1172,  
756 <https://doi.org/10.1007/s00376-012-1266-x>, 2013.

757 Zhao, L., Zhao, C., Wang, Y., Wang, Y., and Yang, Y.: Evaluation of cloud microphysical  
758 properties derived from MODIS and Himawari-8 using in situ aircraft measurements over

759 the Southern Ocean, *Earth Space Sci.*, 7, e2020EA001137,  
760 <https://doi.org/10.1029/2020EA001137>, 2020.

761 Zheng, B., Tong, D., Li, M., Liu, F., Hong, C., Geng, G., Li, H., Li, X., Peng, L., Qi, J., Yan,  
762 L., Zhang, Y., Zhao, H., Zheng, Y., He, K., and Zhang, Q.: Trends in China's anthropogenic  
763 emissions since 2010 as the consequence of clean air actions, *Atmos. Chem. Phys.*, 18,  
764 14095-14111, <https://doi.org/10.5194/acp-18-14095-2018>, 2018.

765 Zhong, J., Zhang, X., Wang, Y., Liu, C., and Dong, Y.: Heavy aerosol pollution episodes in  
766 winter Beijing enhanced by radiative cooling effects of aerosols, *Atmos. Res.*, 209, 59-64,  
767 <https://doi.org/10.1016/j.atmosres.2018.03.011>, 2018.

768 Zhou, B. and Ferrier, B. S.: Asymptotic Analysis of Equilibrium in Radiation Fog, *J. Appl.*  
769 *Meteorol. Clim.*, 47, 1704-1722, <https://doi.org/10.1175/2007jamc1685.1>, 2008.

770 Zhu, J., Zhu, B., Huang, Y., An, J., and Xu, J.: PM<sub>2.5</sub> vertical variation during a fog episode in  
771 a rural area of the Yangtze River Delta, China, *Sci. Total Environ.*, 685, 555-563,  
772 <https://doi.org/10.1016/j.scitotenv.2019.05.319>, 2019.

773  
774  
775  
776  
777  
778  
779  
780  
781  
782  
783  
784  
785  
786



787

**Table 1.** Summary of major parameterisation schemes.

Scheme	Option
Microphysics	Morrison
Boundary layer	MYNN
Short-wave radiation	Goddard
Long-wave radiation	RRTMG
Cumulus	Grell 3D
Aerosol chemistry	MOSAIC (4 bins)
Gas phase chemistry	CBMZ

788

789

790

791

792

793

794

795

796

797

798

799 **Table 2.** Evaluation of PM<sub>2.5</sub> mass concentration. NMB, NME, MFB, and MFE stand for  
800 normalised mean bias, normalised mean error, mean fractional bias, and mean fractional error,  
801 respectively. Time ‘2514’ (DateHour) indicates 14:00 local standard time (LST) (LST =  
802 Universal Time Coordinated + 8 h) on 25 November 2018. The other time expressions follow  
803 the same notation.

DateHour	NMB (%)	NME (%)	MFB (%)	MFE (%)
2514-2614	13	25	13	24
2614-2714	38	42	35	38
Total	25	30	24	28

804

805

806

807

808

809

810

811

812

813

814

815

816

**Table 3.** Elements a–d in the Heidke skill score calculation

	Fog observed	No fog observed
Fog simulated	a	b
No fog simulated	c	d

817

818

819

820

821

822

823

824

825

826

827

828

829

830

831

832 **Table 4.** Quantitative estimation of ACI strength in two fog events (Fog1 and Fog2), including  
833 the responses of fog optical depth ( $\tau_c$ ), liquid water path (LWP), and fog effective radius ( $R_e$ )  
834 to the changes in fog droplet number concentration ( $N_d$ ). In EXP1, both fog events occur under  
835 polluted conditions, and fog events in EXP2 occur under clean conditions. In EXP3, Fog1  
836 occurs under clean conditions and Fog2 occurs under polluted conditions. The ratio represents  
837 the relative change between Fog1 and Fog2, calculated as  $(\text{Fog2} - \text{Fog1})/\text{Fog1}$ . In the fourth  
838 and sixth columns, Fog1 in both EXP2 and EXP3 occur under clean conditions.

	EXP1 vs EXP2			EXP3 vs EXP2		
	Fog1	Fog2	Ratio	Fog1	Fog2	Ratio
$\Delta \ln \tau_c / \Delta \ln N_d$	0.98	1.32	34.7%	–	1.17	–
$\Delta \ln LWP / \Delta \ln N_d$	0.76	1.08	42.1%	–	1.00	–
$-\Delta \ln R_e / \Delta \ln N_d$	0.22	0.24	9.1%	–	0.17	–

839

840

841

842

843

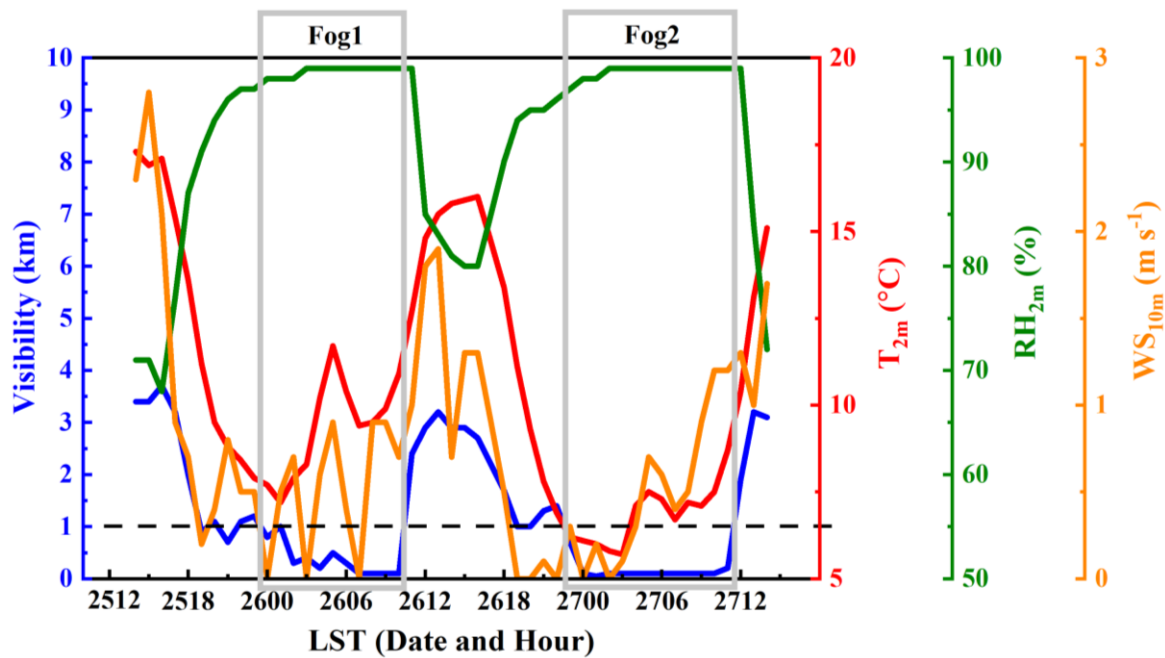
844

845 **Table 5.** Average 2 m relative humidity (RH<sub>2m</sub>) and planetary boundary layer height (PBLH)  
 846 above the ground in domain 03 during 12:00–20:00 local standard time (LST) (LST = Universal  
 847 Time Coordinated + 8 h) on 25 and 26 November 2018 under clean and polluted conditions.  
 848 DIF is the difference in each property between 25 and 26 November.

	Clean			Polluted		
	25 Nov	26 Nov	DIF	25 Nov	26 Nov	DIF
RH <sub>2m</sub> (%)	76	80	4	76	82	6
PBLH (m)	669	610	−59	670	578	−92

849

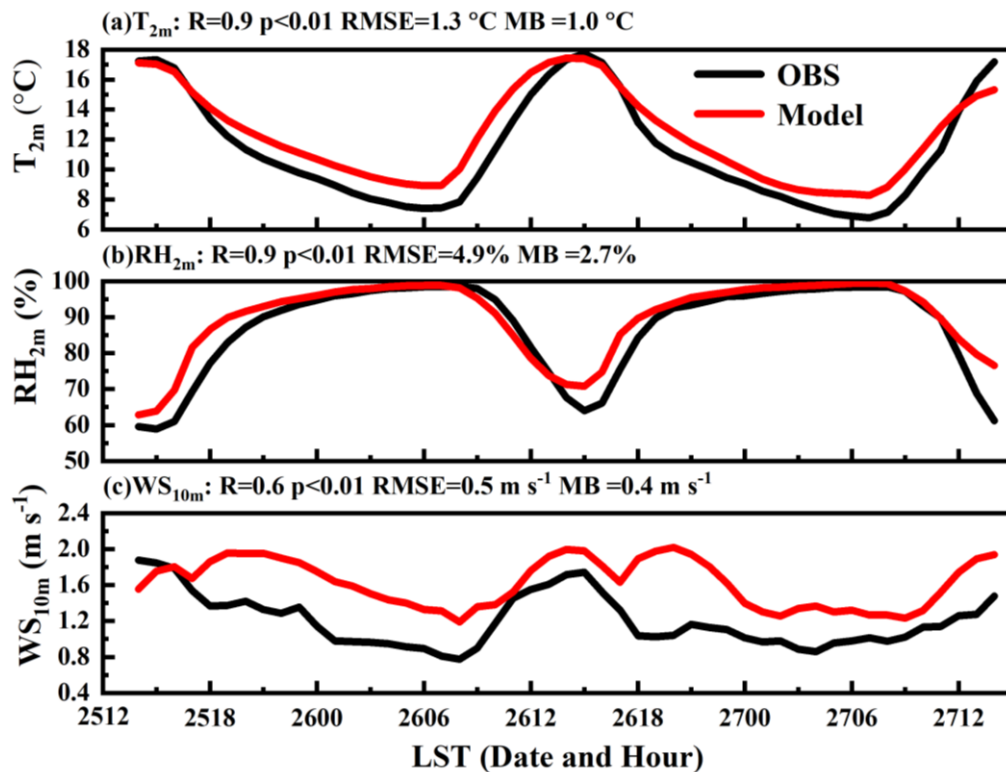
850



851

852 **Figure 1.** The timeseries of visibility, 2 m temperature ( $T_{2m}$ ), 2 m relative humidity ( $RH_{2m}$ ),  
 853 and 10 m wind speed ( $WS_{10m}$ ) above the ground at the Nanjing observation site ( $31.93^{\circ}N$ ,  
 854  $118.9^{\circ}E$ ). Fog1 and Fog2 in the light grey box are the two fog events. Time ‘2512’ indicates  
 855 12:00 local standard time (LST) (LST = Universal Time Coordinated + 8 h) on 25 November  
 856 2018. The other time expressions follow the same notation.

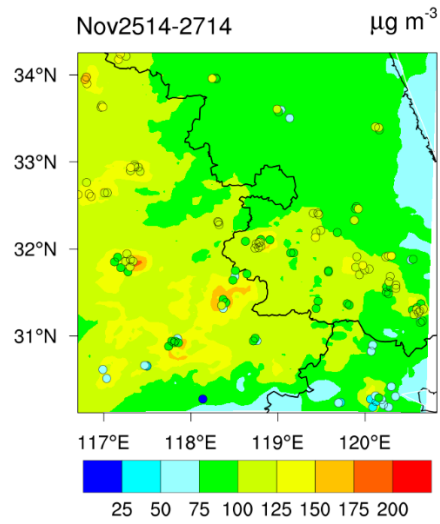
857



858

859 **Figure 2.** Hourly variations in observed (black lines) and simulated (red lines) meteorological  
 860 properties, including (a) 2 m temperature ( $T_{2m}$ ), (b) 2 m relative humidity ( $RH_{2m}$ ), and (c) 10 m  
 861 wind speed ( $WS_{10m}$ ) above the ground, averaged over 104 meteorological stations in domain  
 862 03 from 14:00 local standard time (LST) (LST = Universal Time Coordinated + 8 h) on 25  
 863 November to 14:00 LST on 27 November 2018. R, p, RMSE, and MB indicate the correlation  
 864 coefficient, significance level, root-mean-square error, and mean bias, respectively. The  
 865 equations for RMSE and MB (Eq. S1-S2) are given in the supplement. Time ‘2512’ indicates  
 866 12:00 LST on 25 November 2018. The other time expressions follow the same notation.

867

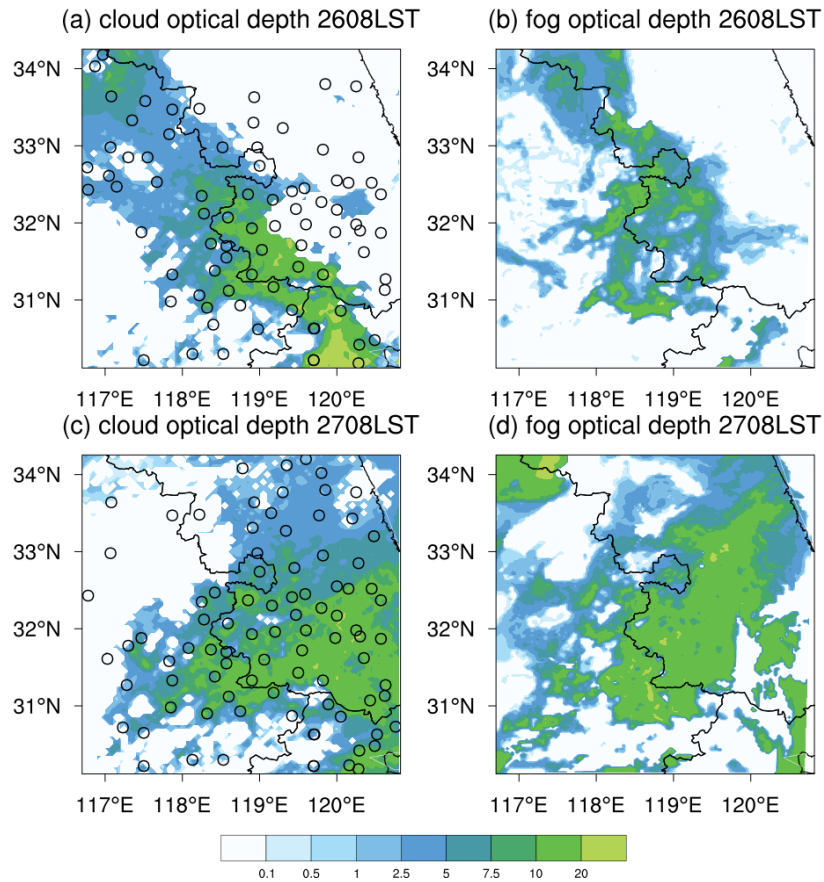


868

869 **Figure 3.** Simulated (shaded area) and observed (coloured dots) average distributions of PM<sub>2.5</sub>  
870 concentration ( $\mu\text{g m}^{-3}$ ) from 14:00 local standard time (LST) (LST = Universal Time  
871 Coordinated + 8 h) on 25 November to 14:00 LST on 27 November 2018.

872





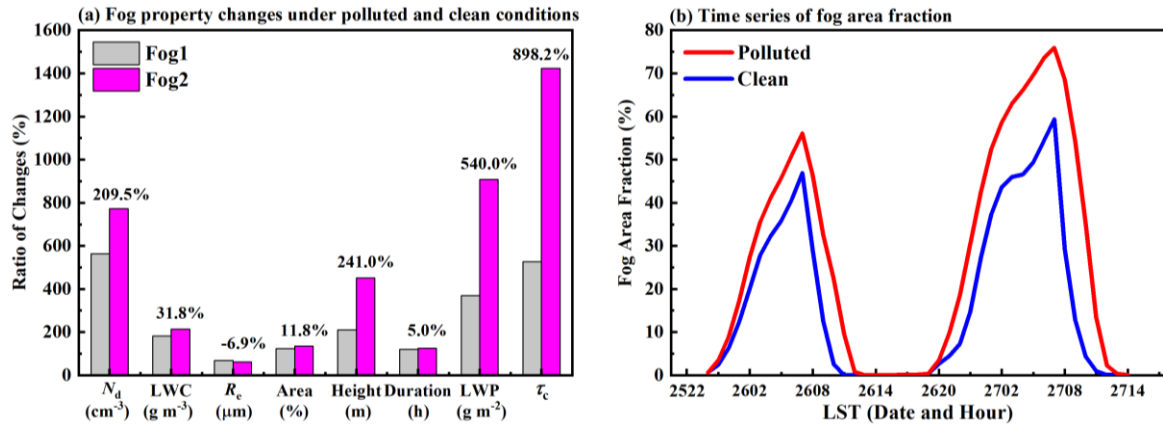
873

874 **Figure 4.** (a, c) Distributions of ground-based fog observations (the black circular points) and  
 875 cloud optical depth from Himawari-8 products at 08:00 LST on 26 and 27 November 2018. (b,  
 876 d) Simulated fog optical depth distributions in domain 03 at the corresponding time of  
 877 observations. Time ‘2608LST’ indicates 08:00 local standard time (LST) (LST = Universal  
 878 Time Coordinated + 8 h) on 26 November 2018. The other time expressions follow the same  
 879 notation.

880

881

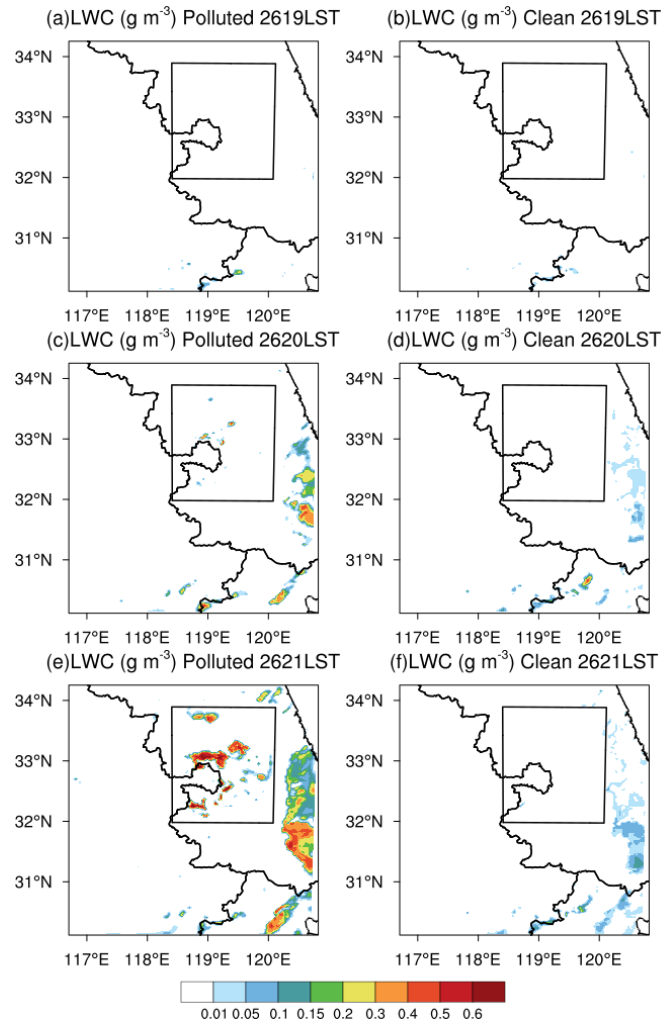
882



883

884 **Figure 5.** (a) Aerosol-induced changes in macro- and microphysical properties during the first  
 885 fog (Fog1) and the second fog (Fog2) events under polluted and clean conditions. (b) Temporal  
 886 evolution of fog area fraction under clean and polluted conditions.  $N_d$ , LWC,  $R_e$ , Area, Height,  
 887 Duration, LWP, and  $\tau_c$  indicate fog droplet number concentration, liquid water content,  
 888 effective radius, fog area fraction, fog-top height, liquid water path, and fog optical depth,  
 889 respectively. The ratios of changes are calculated by Polluted/Clean in Fig. 5a which reveal the  
 890 aerosol-induced changes. The numbers above the bars in Fig. 5a represent the difference in  
 891 those ratios of changes between Fog1 and Fog2 (calculated by Fog2–Fog1). Time ‘2522’ in Fig.  
 892 5b indicates 22:00 local standard time (LST) (LST = Universal Time Coordinated + 8 h) on 25  
 893 November 2018. The other time expressions follow the same notation.

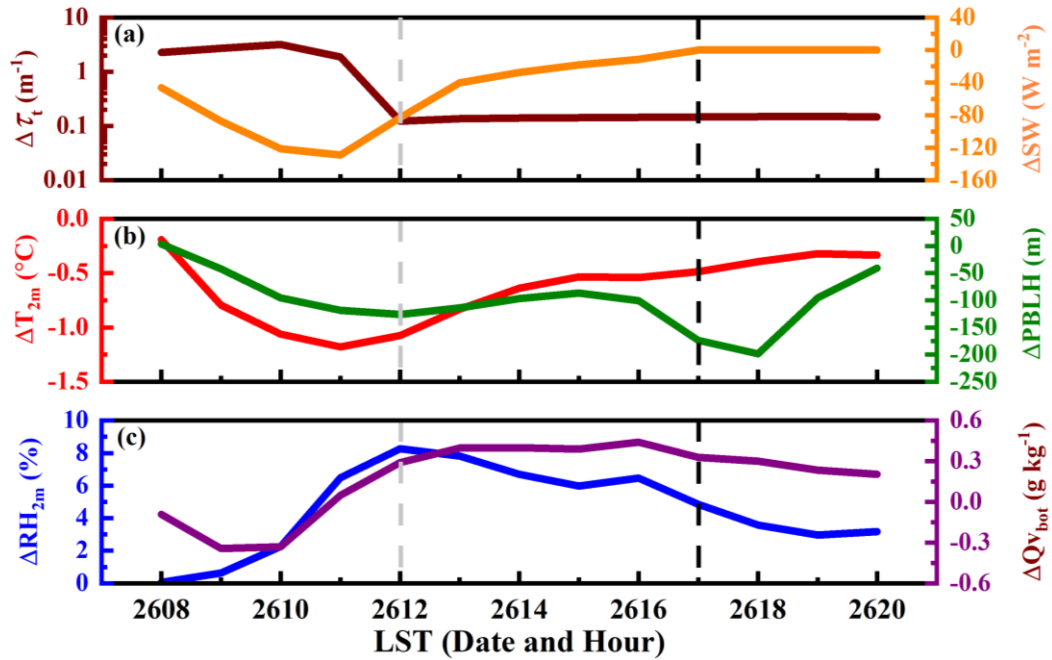
894



895

896 **Figure 6.** Liquid water content (LWC) distribution at the bottom layer from 19:00-21:00 local  
 897 standard time (LST) (LST = Universal Time Coordinated + 8 h) on 26 November 2018 under  
 898 (a, c, e) polluted and (b, d, f) clean conditions. The black box is the area in which Fog2 formed  
 899 earlier under polluted conditions. Time '2619LST' indicates 19:00 LST on 26 November 2018.  
 900 The other time expressions follow the same notation.

901

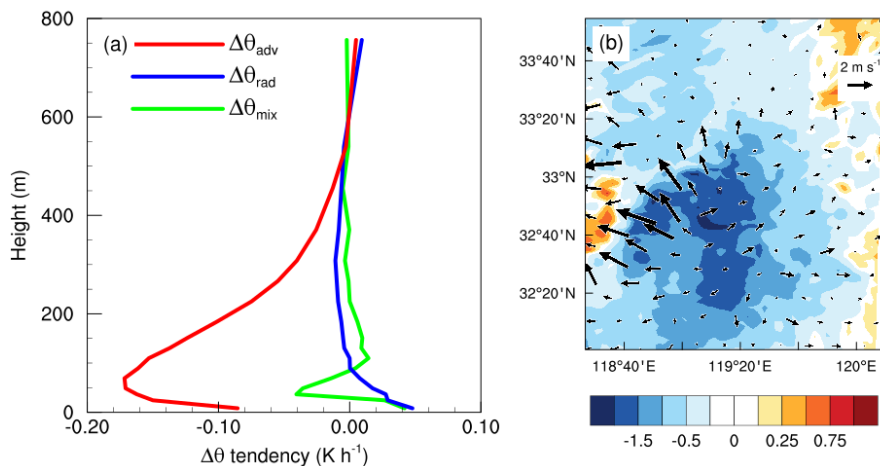


902

903 **Figure 7.** Differences in properties between polluted and clean conditions in the black box in  
 904 Fig. 6, including (a) total optical depth ( $\tau_t$ ), surface downwelling short-wave radiation (SW), (b)  
 905 2 m temperature ( $T_{2m}$ ), planetary boundary layer height (PBLH), (c) 2 m relative humidity  
 906 ( $\text{RH}_{2m}$ ), and water vapour mixing ratio at the bottom of the model ( $Q_{v\text{bot}}$ ), where  $\tau_t = \tau_c$  (fog  
 907 optical depth) + AOD (aerosol optical depth). The grey dashed line is the time of complete  
 908 evaporation of Fog1 under polluted conditions. The black dashed line is the time of sunset.  
 909 Time '2608' indicates 08:00 local standard time (LST) (LST = Universal Time Coordinated +  
 910 8 h) on 26 November 2018. The other time expressions follow the same notation.

911

Average during 17:00-19:00 LST before fog formation



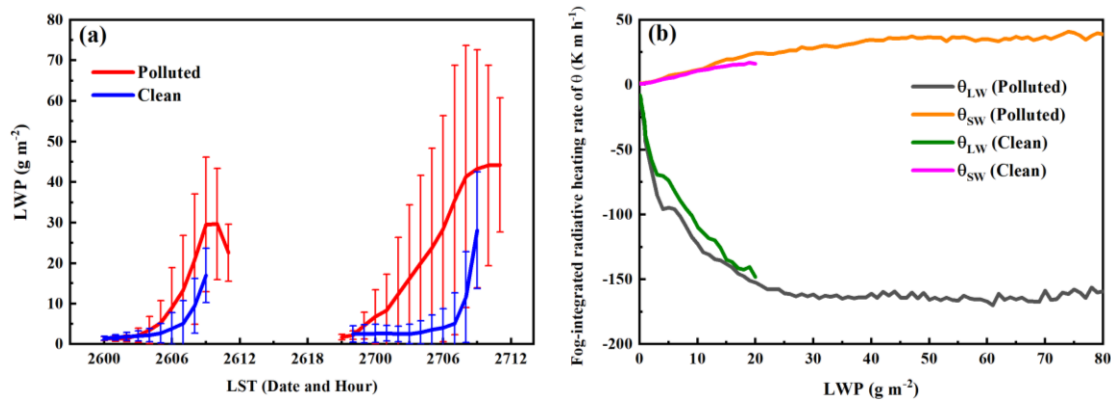
912

913 **Figure 8.** (a) Differences (Polluted – Clean) in terms contributing to the potential temperature  
914 tendency, including radiation ( $\theta_{\text{rad}}$ ), vertical mixing ( $\theta_{\text{mix}}$ ), and advection ( $\theta_{\text{adv}}$ ) in the black box  
915 in Fig. 6 before fog formation (17:00–19:00 local standard time [LST = Universal Time  
916 Coordinated + 8 h]). (b) The shaded area represents the mean temperature difference (Polluted  
917 – Clean), and vectors represent the mean wind vector difference (Polluted – Clean) at the  
918 bottom of the model.

919

920

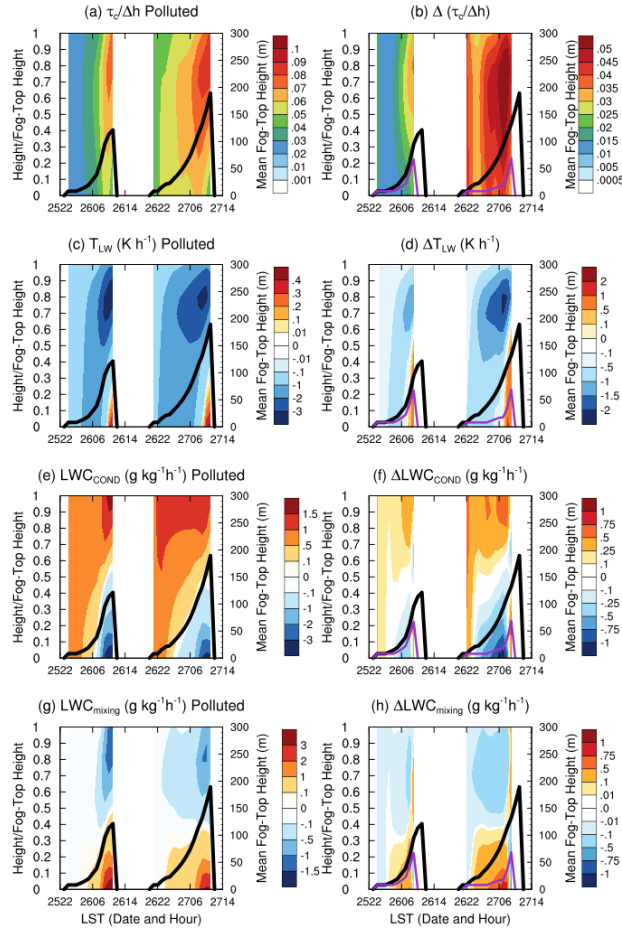
921



922

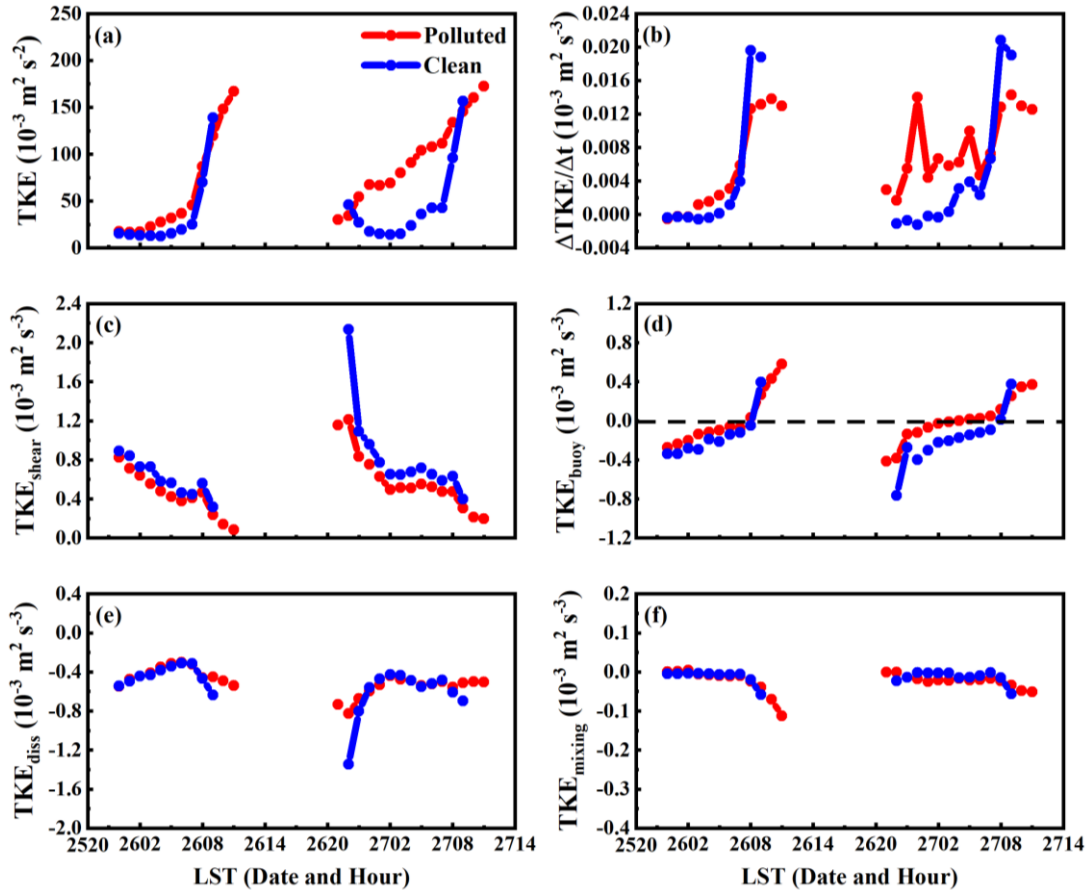
923 **Figure 9.** (a) The timeseries of liquid water path (LWP) under polluted and clean conditions.  
 924 The length of the bar represents standard deviation. (b) Dependence of fog-integrated radiative  
 925 cooling or heating with LWP under polluted and clean conditions.  $\theta_{\text{LW}}$  and  $\theta_{\text{SW}}$  represent  
 926 vertically integrated heating rate of potential temperature ( $\theta$ ) within the fog layer due to long-  
 927 wave radiation and short-wave radiation, respectively. Time '2512' indicates 12:00 local  
 928 standard time (LST) (LST = Universal Time Coordinated + 8 h) on 25 November 2018. The  
 929 other time expressions follow the same notation.

930



931

932 **Figure 10.** Time-height profiles of (a-b) average extinction coefficient through the fog layers,  
 933 which is fog optical depth ( $\tau_c$ ) at per unit height ( $\tau_c/\Delta h$ ), (c-d) radiative cooling rate ( $T_{LW}$ ), (e-f)  
 934 condensation growth rate ( $LWC_{COND}$ ), and (g-h) liquid water content tendency due to vertical  
 935 mixing ( $LWC_{mixing}$ ). Heights on the left axes are normalised by the fog-top heights and the left  
 936 axes are mean fog-top heights. The left column represents polluted conditions and the right  
 937 column represents the difference (Polluted – Clean). Black and purple lines are the mean fog  
 938 top heights under polluted and clean conditions, respectively. Time ‘2522’ indicates 22:00 local  
 939 standard time (LST) (LST = Universal Time Coordinated + 8 h) on 25 November 2018. The  
 940 other time expressions follow the same notation.

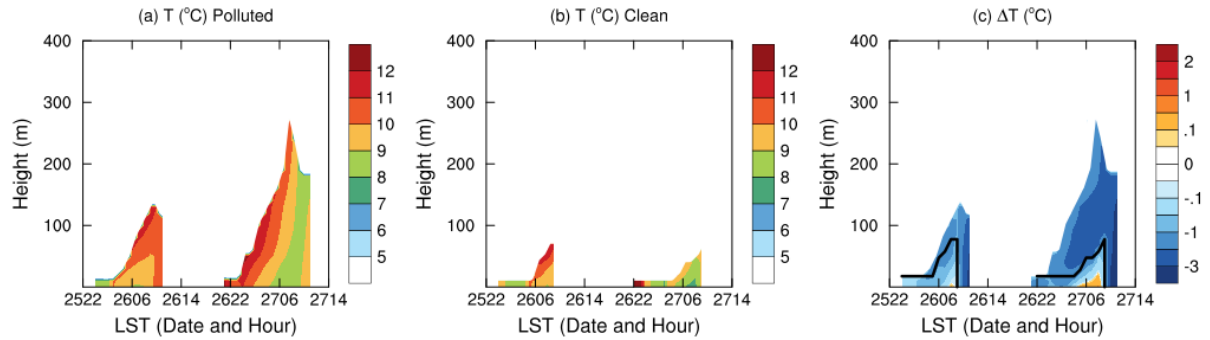


942

943 **Figure 11.** (a) Temporal evolution of turbulent kinetic energy (TKE), (b) TKE tendency, (c)  
 944 wind shear term ( $TKE_{\text{shear}}$ ), (d) buoyancy term ( $TKE_{\text{buoy}}$ ), (e) dissipation term ( $TKE_{\text{diss}}$ ), and (f)  
 945 vertical mixing terms ( $TKE_{\text{mixing}}$ ) under polluted and clean conditions. The dashed line  
 946 represents the zero line for  $TKE_{\text{buoy}}$ . Time ‘2522’ indicates 22:00 local standard time (LST)  
 947 (LST = Universal Time Coordinated + 8 h) on 25 November 2018. The other time expressions  
 948 follow the same notation.

949

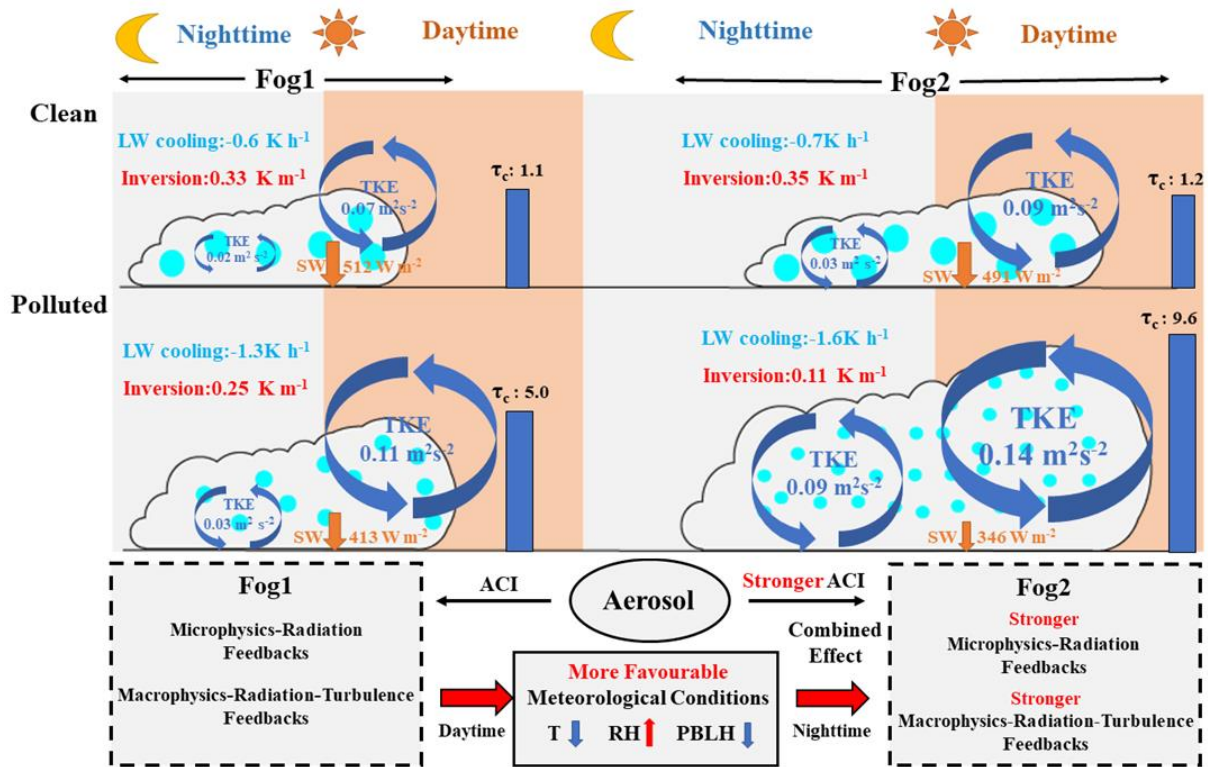




950

951 **Figure 12.** Time-height profiles of in-fog temperature (T) under (a) polluted and (b) clean  
 952 conditions. (c) Difference between polluted and clean conditions. The Black line on the right  
 953 side represents the maximal fog-top height under clean conditions. Time ‘2522’ indicates 22:00  
 954 local standard time (LST) (LST = Universal Time Coordinated + 8 h) on 25 November 2018.  
 955 The other time expressions follow the same notation.

956



957

958 **Figure 13.** Conceptual image of interactions between aerosol–fog interaction (ACI) and  
 959 planetary boundary layer (PBL).  $\tau_c$ , SW, LW, TKE, T, RH, and PBLH stand for fog optical  
 960 depth, short-wave radiation, long-wave radiation, turbulent kinetic energy, temperature, relative  
 961 humidity, and planetary boundary layer height, respectively. LW and inversion are calculated  
 962 at night time, and  $\tau_c$  is calculated at daytime.

963

964